Sharp cell-type boundaries emerge from temporal coordination between morphogen signals

Authors:

Ruiqi Li[1,2,13], Yiqun Jiang[3,4,13], Sarah Platt[3,13], Tianchi Xin[5], Ryan Driskell[6], Kevin A. Peterson[7], Sarah Van[3], Hainan Lam[3], Shagun Lukkad[3], Eva-LaRue Barber[3], Chae Ho Lim[8], M. Mark Taketo[9], Yuval Kluger[1,2,10,11], Peggy Myung[2,3,4,12*]

*Corresponding author

Affiliations:

[1]Computational Biology & Biomedical Informatics Program, Yale University, New Haven, CT 06520, USA

[2]Department of Pathology, Yale University, New Haven, CT 06520, USA

[3]Department of Dermatology, Yale University, New Haven, CT 06520, USA

[4]Molecular, Cellular and Developmental Biology, Yale University, New Haven, CT 06520, USA

[5]Department of Genetics, Yale University, New Haven, CT 06520, USA

[6] School of Molecular Biosciences, Washington State University, Pullman, WA, USA

[7]The Jackson Laboratory, Bar Harbor, ME 04609, USA

[8]Ronald O. Perelman Department of Dermatology, and Department of Cell Biology, NYU Grossman School of Medicine, New York, NY, USA

[9]Colon Cancer Project, Graduate School of Medicine, Kyoto University, Sakyo, Kyoto 606-8501, Japan

[10]Applied Mathematics Program, Yale University, New Haven, CT 06511, USA

[11]Yale Cancer Center, New Haven, CT 06520, USA

[12]Yale Stem Cell Center, New Haven, CT 06520, USA

[13]These authors contributed equally

Keywords: Morphogen, patterning, development, scRNA-sequencing, Wnt, Hedgehog, skin, cell cycle, differentiation

Abstract

Classic models of the French flag problem depict sharp cell-type boundaries emerging from threshold responses to morphogen gradients. Yet, how such boundaries arise during dynamic cell-state transitions remains unclear. We use hair follicle dermal condensates to study a sharp cell-type transition in which proliferative progenitors synchronously undergo cell-cycle exit and molecular differentiation. Using genetic and genomic approaches, we show that Wnt and Hedgehog signaling interact to coordinate the timing of these processes. When their activities are temporally aligned, intermediate transitional states are compressed through cell-cycle exit, producing a sharp cell-type boundary; when misaligned, transitional states expand, yielding fuzzy borders. Mechanistically, elevated Wnt activity promotes cell-cycle exit by regulating chromatin binding of the Hedgehog mediator GLI3. Hedgehog signaling induces differentiation genes in a Wnt-dependent manner and simultaneously elevates Wnt activity, aligning arrest and differentiation in time. These findings reveal a mechanism wherein morphogen interactions coordinate transitions to generate precise cell-type boundaries.

Introduction

Developing tissues must position distinct cell types across space and time to assemble functional organs. How such patterns form was framed by Lewis Wolpert as the “French flag” problem, in which discrete cell types emerge at defined positions along a morphogen gradient (Fig. 1a)[1]. In this framework, graded morphogen signals are interpreted through concentration thresholds that delineate spatial domains of cell fate[2-6]. Yet, a fundamental question remains unresolved: how sharp cell-type boundaries emerge *in vivo* when the underlying signals and cell states vary continuously across a tissue. In developing systems, boundaries do not arise from instantaneous fate switches. Instead, cells progress through dynamic transitions and pass through intermediate states before committing to a new identity. Moreover, in many mammalian tissues, these fate transitions unfold while cells continue to proliferate, raising the question of how ongoing cell-cycle dynamics are coordinated with graded morphogen inputs. Thus,

boundary sharpness may not only reflect where fate thresholds are crossed, but how rapidly cells traverse the same underlying developmental progression.

Addressing the temporal dimension of the French flag problem has been challenging, as most approaches to studying cell fate transitions emphasize cell origins or endpoints, rather than intermediate regulatory programs, or can visualize intermediate cell behaviors without molecular resolution[7-11]. We address this problem in a mammalian system by examining hair follicle dermal condensate formation, a uniquely tractable developmental transition in which the principal morphogen signals are known and cell-state progression occurs over a narrow temporal window[12-14].

Dermal condensates are spheroid clusters of quiescent dermal cells that form beneath epithelial hair follicle placodes and are essential for hair follicle development[15-21]. At E13.5, prior to DC formation, Wnt signaling is broadly activated across the upper dermis, forming a gradient that is highest in cells closest to the epidermis[16, 22, 23]. Wnt activity is required but not sufficient for DC formation. Upon placode formation, epithelial cells secrete Sonic Hedgehog (SHH) and additional Wnt ligands, resulting in localized co-activation of Wnt and SHH in underlying dermal cells[21, 24-26]. Together, these signals are necessary and sufficient for DC formation, yet how Wnt and SHH signaling interact to drive the pre-DC-to-DC transition remains unknown, and DCs appear to emerge abruptly with few detectable intermediates.[8, 27, 28].

Previous work has examined how tissue growth and proliferation affect morphogen gradients by shaping field size, ligand distribution, or the scaling of positional information[29-33]. In these frameworks, proliferation is typically considered in terms of how it modifies the signaling environment cells interpret. Many mammalian tissues, however, undergo fate specification while cells continue to divide, introducing an additional constraint, as proliferative expansion of intermediate states becomes a key factor influencing the precision of pattern formation. In this

83 study, we focus on how interacting morphogen signals coordinate cell-cycle exit with
84 differentiation to ensure spatially precise patterning in such proliferative contexts.
85
86 Here, we ask how interacting morphogen signals regulate the progression of a rapid cell-state
87 transition to generate a sharp tissue boundary. By combining *in vivo* genetic perturbations,
88 chromatin profiling, and a single-cell computational framework that disentangles concurrent
89 biological programs, we are able to capture intermediate transcriptional states that are normally
90 difficult to detect and to determine how their timing and spatial extent are regulated by these two
91 pathways *in vivo*[34]. We show that Wnt and SHH differentially control cell-cycle exit and
92 molecular differentiation, and that the temporal coordination of these processes determines
93 whether transitional states are compressed or expanded, thereby controlling boundary
94 sharpness. Mechanistically, we identify cross-regulation of transcription factor occupancy as a
95 key mechanism linking signaling dynamics to cell-cycle exit.
96
97 **Results**
98 **Cell-cycle exit and molecular differentiation are temporally coordinated during dermal**
99 **condensate formation**
100 Prevailing models of the French flag problem posit that distinct cell states are specified by
101 threshold levels of morphogen concentration that vary with distance from a polarized source,
102 predicting that sharp cell-type boundaries arise from spatial differences in morphogen signaling
103 (Fig. 1a). To examine how this model applies to hair follicle dermal condensate (DC) formation,
104 we asked how dermal cell types are spatially organized before and during DC formation. Prior to
105 DC formation, dermal cells are proliferative and lack DC-specific markers (Extended Data Fig.
106 1a). Upon DC formation, DC cells express characteristic differentiation markers, including *Sox2*,
107 *Sox18*, and *Gal*, and undergo cell-cycle exit, as indicated by minimal EdU nucleotide
108 incorporation, while neighboring upper dermal cells that do not express DC genes remain highly
109 proliferative. (Fig. 1b,c and Extended Data Fig. 1b,c).
110

111 Using *in vivo* labeling, we previously showed that DC cells arise from highly proliferative
112 progenitors located in the upper dermis at E13.5 (Extended Data Fig. 1d)[16, 27]. As DC formation
113 initiates, proliferating cells that give rise to DCs become localized to a region surrounding the
114 nascent condensate (peri-DC region) where they express *Dkk1* (Fig. 1c and Extended Data
115 Fig.1c). During the pre-DC–to–DC transition, *Dkk1*$^{+}$ peri-DC cells exit the cell cycle while
116 upregulating DC differentiation genes[27]. Consistent with this, DC marker expression overlapped
117 with the *in vivo* G1/G0 Fucci2 reporter and with expression of the cell-cycle inhibitor *Cdkn1a*
118 (*p21*), with only rare cells expressed *Cdkn1a* in the absence of *Sox2* (Fig. 1c and Extended
119 Data Fig. 1e)[16, 35]. These data indicate that cell-cycle exit and DC differentiation occur
120 concurrently during DC formation.
121
122 Given this temporal coincidence, we next asked how these two processes relate to Wnt and
123 Sonic Hedgehog (SHH) signaling during DC formation. At E13.5, prior to SHH expression, Wnt
124 signaling is active in the upper dermis (Extended Data Fig. 1a,b) but is not sufficient to induce
125 DC gene expression[16, 22, 36]. Using *Lef1* as a canonical readout of Wnt activity, which is
126 concordant with expression of multiple Wnt target genes (*Axin2*, *Wif1*, *Tcf7*) (Extended Data Fig.
127 1f)[16, 27], we examined the relationship between Wnt signaling and proliferation. At E13.5, *Lef1*
128 expression was highest in the most superficial layer of upper dermis and decreased across
129 deeper dermal cell layers, yet this spatial pattern did not correlate with EdU incorporation, nor
130 with DC gene expression (Extended Data Fig. 1a).
131
132 By E14.5, SHH expression in placode cells resulted in SHH activation in the underlying dermis.
133 At this stage, dermal SHH activity (assessed by *Ptch1*) covaried with Wnt signaling (*Lef1*)
134 across dermal populations, with significantly higher *Lef1* levels detected compared to E13.5
135 (Fig. 1d). The highest levels of both signals were observed in DC cells, intermediate levels in
136 peri-DC (*Dkk1*$^{+}$) progenitors, and progressively lower levels in surrounding upper dermal cells.
137 In contrast to E13.5, elevated Wnt activity at E14.5 correlated with reduced proliferation, with
138 the lowest EdU incorporation observed in DC cells (Fig. 1d,e). Thus, quiescence and molecular

139 differentiation coincide spatially and temporally within a narrow domain characterized by
140 elevated Wnt and SHH signaling.
141
142 **High Wnt activity induces cell-cycle exit independently of SHH signaling**
143 To dissect the respective contributions of Wnt and SHH signaling to the pre-DC–to-DC
144 transition, we perturbed each pathway prior to DC formation. Because both pathways are
145 required for DC differentiation, standard loss-of-function approaches preclude analysis of their
146 individual roles at this stage. Given that DC cells ultimately exhibit the highest levels of both Wnt
147 and SHH activity, we asked whether these signals contribute to distinct components of the
148 transition or act through a shared mechanism. We therefore examined the effects of elevating
149 Wnt signaling at E13.5, prior to DC formation by expressing a constitutively active form of β-
150 catenin (*Axin2CreER;βcat*$^{fl/EX3}$, hereafter Actβcat; Fig. 2a, tamoxifen at E11.5).
151
152 To unbiasedly assess how increased Wnt activity reshapes dermal transcriptional states before
153 DC differentiation, we performed single-cell RNA sequencing on E13.5 Actβcat and control
154 dermis. Dermal cells were filtered for analysis using established markers (e.g., *Col1a1*,
155 *PDGFRα*)[16, 27]. Consistent with prior work, Actβcat mutant dermal cells showed increased
156 expression of Wnt target genes, including *Lef1*, *Axin2* and *Tcf7*, but not DC markers (e.g., *Sox2*)
157 or SHH target genes (e.g., *Gli1*) (Fig. 2b). Notably, differential gene expression analysis
158 revealed that *Cdkn1a*, a cell-cycle inhibitor normally expressed in DC cells at E14.5, was among
159 the most significantly upregulated genes in E13.5 Actβcat dermal cells (Fig. 2b and
160 Supplementary Table 1). Quantitative FISH confirmed elevated *Lef1* expression in E13.5
161 Actβcat dermal cells relative to controls and showed that Wnt target gene levels did not exceed
162 those observed in wildtype DC cells, indicating that activated β-catenin elevates Wnt signaling
163 but not above physiological levels (Fig. 2c and Extended Data Fig. 2a). FISH analysis further
164 showed that constitutive Wnt activation was sufficient to induce expression of *Cdkn1a* (*p21*) at
165 E13.5 in the absence of SHH activation, and *Cdkn1a*+ cells exhibited reduced EdU
166 incorporation (Fig. 2c).

167

168 By E14.5, DCs were present in both control and Actβcat embryos but were enlarged in mutants
169 (Extended Data Fig. 2b). In control embryos, *Cdkn1a* expression was largely restricted to *Sox2*+
170 DC cells, whereas in Actβcat mutants, it extended into surrounding *Sox2*- upper dermal cells
171 (Fig. 2d). Both *Sox2*+ and *Sox2*− cells expressing high *Cdkn1a* exhibited low EdU incorporation
172 (Fig. 2d). *Sox2*+ cells in Actβcat mutants were closest to placodes and expressed the highest
173 levels of *Ptch1*, whereas surrounding mutant *Cdkn1a*+*Sox2*- cells expressed lower *Ptch1* levels,
174 indicating that DC gene expression requires SHH signaling above a defined threshold (Fig. 2e).
175 Thus, elevated Wnt signaling is sufficient to induce cell-cycle exit in the absence of SHH,
176 whereas molecular DC differentiation requires additional SHH-dependent input (Fig. 2f).
177

178 **SHH signaling cell-autonomously elevates Wnt activity coincident with cell-cycle exit**
179 Our results show that elevated Wnt activity induces cell-cycle exit without DC differentiation. We
180 next examined how SHH signaling influences this transition. Specifically, we asked whether
181 elevated SHH activity could initiate DC gene expression independently of cell-cycle exit. To
182 address this, we expressed a constitutively activated form of Smoothened
183 (*Axin2CreER;RosaLSL-Smom2YFP*, hereafter ActSMO) in the dermis prior to DC formation
184 when Wnt signaling levels are low (tamoxifen E11.5; Fig. 3a). Whole-mount analysis of E14.5
185 skin showed that high SHH activation in Wnt-active dermal cells induced large dermal clusters
186 expressing DC genes in the upper dermis (Fig. 3b). These clusters formed autonomously
187 without placodes, indicating that DC gene expression can occur in the absence of placode-
188 derived Wnt ligands[27]. Notably, many cells in the outer layers of Sox2+ dermal clusters
189 remained proliferative, as indicated by %Sox2+/EdU+ double labeling, demonstrating that DC
190 gene expression can occur independently of cell-cycle arrest. By contrast, Sox2+ cells in the
191 center of clusters lacked EdU incorporation similar to quiescent DC cells in wildtype embryos.
192

193 Given the observed quiescent central Sox2+ dermal cells (Fig. 3b), we asked whether there
194 were similar molecular changes to those seen in the E13.5 Actβcat mutant. We obtained

195 scRNA-seq data from E13.5 ActSMO and paired control skin (Fig. 3c). As expected, E13.5
196 ActSMO dermal cells exhibited uniformly high *Ptch1* expression. *Lef1* expression remained
197 largely enriched in upper dermal (UD) cells but was significantly elevated compared to E13.5
198 controls (Fig. 3c,d). FISH analysis confirmed increased *Lef1* expression in E13.5 ActSMO
199 dermis despite the absence of placodes (Fig. 3d). Importantly, only *Ptch1*+ cells (recombined)
200 showed elevated *Lef1* expression, while neighboring *Ptch1*-negative cells (non-recombined)
201 retained normal *Lef1* levels comparable to E13.5 control UD cells, indicating a cell-autonomous
202 effect. ActSMO cells with high *Lef1* expression also exhibited elevated *Cdkn1a* expression and
203 low rates of EdU incorporation (Fig. 3d,e). Together, these findings show that SHH activation
204 elevates Wnt signaling cell-autonomously and is associated with induction of cell-cycle exit,
205 independent of placode Wnt ligands (Fig. 3f).
206
207 **GeneTrajectory resolves transcriptional programs associated with cell-cycle exit**
208 In the ActSMO condition, DC genes are expressed in cells that remain proliferative (Fig. 3b),
209 indicating that cell-cycle exit and DC gene expression can be temporally uncoupled. To resolve
210 the gene programs underlying these processes, we applied GeneTrajectory (GT), a
211 computational approach that separates co-occurring transcriptional programs from whole
212 transcriptome scRNA-seq data[34]. Unlike conventional pseudotime methods that assign cells to a
213 single lineage trajectory, GT directly constructs gene trajectories, allowing individual cells to be
214 analyzed across multiple overlapping biological processes.
215
216 We first applied GT to E14.5 wildtype dermal scRNA-seq data, identifying three gene
217 trajectories, corresponding to proliferation (S/G2/M), DC differentiation and lower dermal
218 differentiation (Fig. 4a). The DC trajectory was partitioned into stages using gene bins, and cells
219 were visualized by gene bin scores (Fig. 4a and Extended Data Fig. 3a)[34]. *Lef1* and *Ptch1*
220 expression covaried across DC trajectory stages, with maximal expression at the terminal stage
221 6 (Fig. 4b and Extended Data Fig. 3b). Canonical DC genes, including *Gal*, *Sox18* and *Sox2,*
222 were similarly enriched at stage 6 (Fig. 4c). Cell-cycle analysis revealed that stage 6 cells were

223 quiescent with a G1 fraction near 1.0, and elevated *Cdkn1a* expression (Fig. 4c). Thus, in the
224 wildtype condition, cell-cycle exit and molecular DC differentiation coincide at the terminus of
225 the DC trajectory.
226
227 We next applied GT to E13.5 ActSMO scRNA-seq data in which cell-cycle exit and DC
228 differentiation are uncoupled. GT identified four trajectories (Fig. 4d and Extended Data Fig. 3c).
229 Two were similar to the control, corresponding to proliferation (S/G2/M) and LD differentiation.
230 Two additional trajectories were unique to the ActSMO dermis: one containing DC genes and a
231 second lacking DC markers. Cells expressing this latter program localized to a subset of Wnt-
232 active cells and were largely restricted to G1/G0 phase (Fig. 4e and 3c). Pathway analysis
233 revealed enrichment for TP53-associated cell-cycle inhibitory genes, including *Trp53inp1* and
234 *Plk2,* overlapping with *Cdkn1a* expression (Fig. 4f and Supplementary Table 1). FISH analysis
235 confirmed significant upregulation of both *Cdkn1a* and *Trp53inp1* in the E13.5 ActSMO dermis
236 relative to controls (Fig. 4g and 3d and Extended Data Fig. 3d)
237
238 In ActSMO mutants, SHH-active cells expressing *Trp53inp1* exhibited significantly higher *Lef1*
239 levels than control upper dermal cells (Fig. 4g), consistent with earlier results showing that SHH
240 elevates Wnt activity and promotes quiescence (Figs. 3d and 2c). To test whether elevatd Wnt
241 signaling alone induces this TP53-associated program, we applied GT to the E13.5 Actβcat
242 dermis, which induces *Cdkn1a* but not DC genes (Extended Data Fig. 3e). GT analysis
243 identified a similar *Trp53inp1*-containing program in E13.5 Actβcat mutants (Supplementary
244 Table 1). We applied a module projection (label transfer) method to assess whether the gene
245 program was shared across different perturbations. Specifically, we transferred the E13.5
246 ActSMO-specific trajectory onto E13.5 Actβcat and control datasets, which revealed a shared
247 molecular state in both mutants that was absent in controls (Fig. 4h).
248
249 To determine whether this program reflects a general consequence of reduced proliferation, we
250 analyzed E13.5 Wntless conditional knockout (*K14Cre;Wls*$^{fl/fl}$) embryos in which epidermal Wnt

251 ligand secretion is disrupted, resulting in loss of dermal Wnt signaling and reduced dermal
252 proliferation (Extended Data Fig. 3f)[22, 34, 37]. Label transfer of the ActSMO/Actβcat-specific
253 trajectory was not detected in Wntless cKO dermis (Fig. 4h and Extended Data Fig. 3f),
254 indicating that this TP53-associated program is Wnt-dependent and specific to DC-associated
255 cell-cycle exit.
256
257 Finally, we examined the cell-cycle dynamics of cells expressing this gene program. At E13.5
258 and E14.5, most ActSMO *Trp53inp1*+ cells showed low EdU incorporation comparable to
259 quiescent DC cells (Fig. 4i and Extended Data Fig. 4a). EdU pulse-chase experiments
260 demonstrated that a substantial fraction of *Trp53inp1*+ cells retained EdU nucleotide similarly to
261 wildtype DCs (Fig. 4i and Extended Data Fig.1d)[16, 27]. Although ActSMO dermal clusters
262 contained proliferating Sox2+ cells at E14.5, most became quiescent by E15.5 (Extended Data
263 Fig. 4b), indicating that these proliferating cells exit the cell cycle after division. Together, these
264 data define a shared transcriptional program underlying cell-cycle exit during the pre-DC-to-DC
265 transition, which we term the *"Exit" gene trajectory*.
266
267 **Loss of GLI3 chromatin binding induces cell-cycle exit downstream of elevated Wnt**
268 **signaling**
269 Although Wnt activity is required for dermal proliferation, our results indicate that elevated Wnt
270 activity promotes cell-cycle exit during DC formation[16, 22]. To examine the underlying
271 mechanism, we profiled genes differentially bound by CTNNB1 (β–catenin) in E13.5 Actβcat
272 and control dermis. CTNNB1 binding was enriched at canonical Wnt target genes (e.g., *Sp5*,
273 *Axin2*, *Lef1*), but not at *Cdkn1a,* Exit GT genes, or other loci associated with cell cycle inhibition
274 (Extended Data Fig. 5a,b)[22]. These findings raised the question of how elevated Wnt activity
275 promotes cell-cycle exit despite the absence of direct CTNNB1 binding at cell-cycle inhibitory
276 genes. Given that Wnt activity is elevated upon SHH activation, it was plausible that
277 components of the SHH pathway mediate Wnt-dependent cell-cycle exit. In other tissues, Wnt
278 signaling regulates *Gli3* expression independently of SHH[38]. In the absence of SHH ligand, Gli3

279 is predominantly present in its cleaved repressor form, which binds a broad range of SHH target
280 genes[39, 40]. FISH analysis showed that *Gli3* was expressed in Wnt-active dermal cells in both
281 control and Actβcat embryos at E13.5 prior to SHH expression (Fig. 5a). To profile GLI3 binding,
282 we performed CUT&RUN in E13.5 Actβcat and control dermis using *Gli3Flag* knockin embryos.
283 Interestingly, GLI3 occupancy was globally reduced in the Actβcat condition as indicated by
284 decreased GLI3-bound reads at transcriptional start sites (Fig. 5b). De novo motif analysis
285 confirmed enrichment of GLI motifs at regions showing reduced binding (Extended Data Fig.
286 5c)[41]. These regions were enriched for genes associated with SHH signaling, despite the fact
287 that most canonical SHH target genes (e.g., *Ptch1*, *Gli1*) were not expressed and lacked active
288 histone marks (H3K4me3 or H3K27ac) at E13.5 (Fig. 5c). These observations are consistent
289 with a recent report indicating that GLI3 binding prior to SHH does not actively repress
290 transcription (i.e., is inert) and that many targets become activated only after SHH expression[42].
291 Western Blot analysis confirmed that cleaved Gli3 protein levels were retained in the Actβcat
292 mutant, showing that reduced chromatin occupancy was not due to loss of Gli3 protein and that
293 Gli3 remained predominantly in its cleaved repressor form (Fig. 5d). These results show that
294 elevated Wnt signaling alone reduces GLI3 chromatin occupancy at many genomic regions
295 independently of SHH.
296
297 To test whether loss of GLI3 binding is sufficient to induce cell-cycle exit, we ablated *Gli3* in the
298 dermis (*Axin2CreER;Gli3*$^{fl/fl}$ or Gli3 cKO; tamoxifen E11.5). At E14.5, DCs in Gli3 cKO embryos
299 were smaller than in controls (Fig. 5e), and *Dkk1*+ peri-DC progenitors showed premature
300 upregulation of *Cdkn1a* and reduced EdU incorporation (Fig. 5e and Extended Data Fig. 5d).
301 Similarly, at E13.5 prior to DC formation, Gli3 cKO dermal cells exhibited elevated *Cdkn1a/p21*
302 expression and reduced proliferation, phenocopying the Actβcat condition (Fig. 5f and Extended
303 Data Fig. 5e).
304
305 FISH analysis confirmed reduced *Gli3* expression in the dermis of E13.5 Gli3 cKO embryos,
306 while Wnt target genes were unaffected, suggesting that Gli3 acts downstream of elevated Wnt

307 activity (Fig. 5f and Extended Data Fig. 5f). Canonical SHH target genes (e.g. *Ptch1*) were also
308 not induced, confirming that loss of Gli3 does not broadly derepress SHH targets and that the
309 lack of SHH target expression in the Actβcat condition is unlikely due to residual GLI3
310 repression. To assess whether GLI3 binding is associated with chromatin organization, we
311 performed chromatin capture (Micro-C) in E13.5 wildtype dermis. GLI3-bound loci (e.g., *Ptch1*)
312 were actually modestly enriched in A (open) rather than B (closed) compartments but rarely
313 participated in chromatin loops (<1%) and lacked active promoter marks (Extended Data Fig.
314 5g). By contrast, canonical Wnt target genes (e.g., *Lef1* and *Sp5)* formed chromatin loop
315 interactions and showed active histone modifications (Extended Data Fig. 5g). Moreover,
316 snATAC+RNA-seq analysis of E14.5 embryos that lack epidermal *Shh* showed significant GLI
317 motif accessibility localized to Wnt-active cells even without Gli activator function (Fig. 5g).
318 Together, these data indicate that GLI3 does not actively repress many bound regions and may
319 instead prime GLI sites for accessibility prior to SHH.
320
321 As expected, scRNA-seq analysis of E13.5 Gli3 cKO dermis showed reduced *Gli3* expression.
322 Neither DC nor canonical SHH target genes were detected, and Wnt target genes were retained
323 (Extended Data Fig. 6a,b). GT analysis identified four trajectories in Gli3 cKO dermis, three
324 corresponding to control populations and a fourth absent in controls (Fig. 5h and Extended Data
325 Fig.6c). This trajectory overlapped with the Exit GT identified in the Actβcat and ActSMO
326 mutants and was enriched for cell-cycle inhibitory genes, including *Trp53inp1* (Fig. 5h and
327 Supplementary Table 1). Additionally, label transfer of the Exit GT from the ActSMO mutant to
328 the Gli3 cKO dataset identified a corresponding population that expressed this gene program
329 (Fig. 5i), showing that this Exit gene program is shared across ActSMO, Actβcat, and Gli3 cKO
330 conditions. Using EdU pulse-chase experiments, we found that *Cdkn1a*-high cells in the Gli3
331 cKO were largely quiescent, while representing recent progeny of cell divisions (Extended Data
332 Fig. 5e). Thus, β-catenin and Gli3 function in a common pathway regulating cell-cycle exit.
333 Cross-referencing genes that lost GLI3 binding in E13.5 Actβcat dermis with those upregulated
334 in E13.5 Gli3 cKO dermis identified multiple cell-cycle inhibitory genes, including *Mxd4* and

335 *Efna5*, which showed increased expression and more active promoter marks (Extended Data
336 Fig. 6d). In addition, Exit GT genes such as *Baiap2* and *Cpt1c* also exhibited reduced GLI3
337 binding and increased expression. Together, these data indicate that β-catenin and Gli3 function
338 within a shared pathway regulating cell-cycle exit in which elevated Wnt signaling causes loss of
339 GLI3 chromatin occupancy and induction of genes associated with cell-cycle exit (Fig. 5j).
340
341 **Uniformly high SHH activity induces dermal condensate gene expression across the Wnt**
342 **gradient**
343 High SHH activity can induce DC gene expression before cell-cycle exit, indicating that DC
344 differentiation does not strictly require a preceding quiescent state (Fig. 3b). However, in the
345 wildtype condition, DC genes are induced abruptly as cells exit the cell cycle, suggesting that
346 Wnt activity contributes to the timing of DC gene induction. Given that SHH cell-autonomously
347 elevates Wnt activity, we examined whether Wnt signaling levels modulate how DC genes are
348 induced in response to high SHH activity.
349
350 To address this, we analyzed the DC gene trajectory in the E13.5 ActSMO mutant, in which
351 SHH activity is uniformly high across cells spanning a range of Wnt activity (Fig. 6a and
352 Extended Data Fig 7a). In the E14.5 wildtype DC gene trajectory, DC genes are induced
353 primarily at the terminal stage, coinciding with the highest levels of *Lef1* and *Ptch1* expression
354 (Fig. 4a,c). By contrast, in the ActSMO condition, DC genes, including *Gal*, *Sox18,* and *Sox2*,
355 were induced progressively across DC GT stages, with cumulative expression correlating with
356 increasing *Lef1* levels (Fig. 6b,c,d and Extended Data Fig. 7b). Cells with highest *Lef1* levels
357 showed the most advanced progression along the trajectory and the strongest DC gene
358 expression (Fig. 6c,d).
359
360 Consistent with the requirement for Wnt signaling in DC differentiation, cells with high SHH
361 activity but lacking Wnt signaling in the ActSMO condition failed to express DC genes (Fig. 6c
362 and Extended Data Fig. 7c)[27]. Thus, uniform SHH activation expands the window over which

363 Wnt-competent cells initiate DC gene expression, resulting in graded rather than abrupt
364 induction of DC genes. In both E14.5 wildtype and Actβcat (high Wnt) conditions, DC genes
365 were restricted to Wnt-active cells with high SHH activity, indicating that DC differentiation
366 requires SHH signaling above a defined threshold (Fig. 6e).
367
368 **Coupling Wnt and SHH gradients is sufficient to synchronize the timing of cell-cycle exit**
369 **with molecular differentiation**
370 Given that cell-cycle exit and DC differentiation coincide where high Wnt activity overlaps with
371 SHH signaling, we tested whether coupling these gradients is sufficient to restore temporal
372 coordination between the two processes. In wildtype skin, this overlap occurs in dermal cells
373 adjacent to placodes. We therefore induced epidermal SHH expression at E13.5 (*K14Cre;Rosa-*
374 *LSL-SHH*; SHH OE) to activate SHH signaling in Wnt-active dermal cells prior to placode
375 formation (Fig. 7a)[43, 44]. FISH analysis revealed that *Lef1* and *Ptch1* covaried with dermal depth
376 with the highest levels in cells closest to the epidermis (Fig. 7b). Compared to E13.5 controls,
377 *Lef1* levels were increased in the superficial dermis, indicating that SHH ligand expression
378 enhanced Wnt activity. DC genes (e.g., *Sox2*, *Gal*) were restricted to these superficial layers
379 and coincided with *Cdkn1a* expression and low EdU incorporation (Fig. 7c and Extended Data
380 Fig. 8a). *Dkk1* expression localized to a deeper layer beneath cells expressing DC genes.
381 scRNA-seq analysis of E13.5 SHH OE dermis confirmed overlapping *Lef1* and *Ptch1*
382 expression, with DC genes and *Cdkn1a* restricted to cells with the highest combined signal
383 levels (Fig. 7d).
384
385 GT analysis identified three trajectories corresponding to proliferation, lower dermal
386 differentiation and DC differentiation, mirroring E14.5 wildtype dermis (Figs. 4a and 7e and
387 Extended Data Fig. 8b). Notably, a distinct Exit trajectory was not detected. Within the DC
388 trajectory, *Lef1* and *Ptch1* increased coordinately, and DC genes and *Cdkn1a* were induced
389 synchronously at the terminal stage, coincident with quiescence (Fig. 7f and Extended Data Fig.

390 8c). Thus, coupling Wnt and SHH activity is sufficient to restore the temporal alignment of
391 differentiation and cell-cycle exit.
392
393 Based on our findings in Actβcat mutants, we next asked whether loss of GLI3 chromatin
394 occupancy also occurs when Wnt and SHH signaling are coupled. GLI3 CUT&RUN analysis in
395 SHH OE dermis revealed global depletion of GLI3 binding (Fig. 7g and Extended Data Fig. 8d),
396 indicating that GLI3 displacement is not an artifact of genetic stabilization of β-catenin. Loss of
397 GLI3 binding was observed at cell cycle regulatory genes (*Mxd4* and *Efna5*) associated with
398 active histone marks (Extended Data Fig. 8e). In contrast to Actβcat mutants, SHH target genes
399 (*Ptch1*, *Gli1*) were transcriptionally activated, accompanied by increased H3K4Me3 and
400 H3K27Ac signal. Because SHH signaling converts cleaved GLI3 repressor into full-length GLI
401 activator, both detectable by anti-Flag immunoprecipitation, the observed loss of GLI3
402 occupancy suggests replacement by other GLI activators at SHH target loci (Fig. 7h). These
403 data indicate that GLI3 eviction both derepresses cell-cycle exit genes and may also prime
404 SHH-dependent target loci for activation.
405
406 To test whether graded Wnt and SHH inputs are sufficient to coordinate these processes
407 outside of the *in vivo* tissue context, we reconstituted the system *in vitro* by using E13.5
408 PDGFRαH2BGFP dermal cells competent to respond to both pathways[45]. These cells showed
409 dose-dependent gene responses to the Wnt agonist (CHIR99021) or the Smoothened agonist
410 (SAG) (Extended Data Fig. 9a). SAG enhanced *Lef1* expression in CHIR-treated cells in a
411 manner dependent on baseline Wnt activity (Extended Data Fig. 9b). High doses of CHIR alone
412 induced *Cdkn1a*, whereas combined CHIR and SAG treatment induced DC genes, including
413 *Gal* and *Sox18* (Extended Data Fig. 9c,d).
414
415 Finally, to assess how signal coupling affects DC morphogenesis, E13.5 dermal cells were
416 seeded onto a collagen-based 3D matrix with varying doses of CHIR and/or SAG (Fig. 7i and
417 Extended Data Fig. 9e). High-dose CHIR (5 μM) combined with SAG (50 nM) produced large

418 dermal clusters that expressed Robo2, a gene expressed in DC cells that regulates cell
419 migration and tissue morphogenesis[46, 47]. These clusters showed low proliferation, whereas
420 other conditions showed higher proportions of Ki67+ cells. Thus, coupling high Wnt and SHH
421 activity is sufficient to align molecular differentiation with cell-cycle exit *in vitro*.
422
423 Collectively, these results indicate that the pre-DC–to-DC transition comprises separable
424 biological processes whose timing can be differentially coordinated by Wnt and SHH. These
425 relationships are summarized in 7j.
426
427 **Discussion**
428 In this study, we identify a mechanism by which interacting morphogen signals generate sharp
429 cell-type boundaries by coordinating the timing of separable components of a cell-state
430 transition. During dermal condensate (DC) formation, we show that Sonic Hedgehog (SHH) acts
431 on Wnt-primed cells to elevate Wnt activity, which is sufficient to induce cell-cycle exit through
432 eviction of the transcriptional repressor GLI3 from chromatin, while SHH concurrently initiates
433 the differentiation program. By aligning differentiation with cell-cycle exit, this coordination
434 prevents proliferative expansion of intermediate states, causing transitional cells to remain
435 sparse and difficult to detect. In this way, boundary sharpness reflects regulated temporal
436 compression of a developmental transition, rather than the absence of intermediate cell states.
437 While sharp transitions can also arise from nonlinear ligand diffusion, our findings reveal a
438 distinct mechanism in which interactions between morphogen pathways synchronize concurrent
439 transcriptional programs.
440
441 These findings revisit classic interpretations of the French flag problem, which emphasized fixed
442 concentration thresholds of a polarized morphogen as primary determinants of spatial
443 patterning[2-6, 48]. Our data instead indicate that during DC specification, morphogen thresholds
444 function as triggers that initiate a committed developmental progression. In this context, SHH
445 gates entry into the DC differentiation program, whereas Wnt activity shapes the timing and

446 synchrony of its execution, establishing a division of labor between permissive and kinetic
447 morphogen inputs. Abrupt boundaries therefore emerge not from static positional decoding, but
448 from coordinated progression through a shared cell-state transition, providing a framework for
449 understanding how gradual signaling changes can be converted into abrupt cell-state
450 transitions.
451
452 Although tight coupling of Wnt and SHH activities generates a sharp and synchronous transition
453 during DC formation, variation in the timing, strength, or spatial alignment of interacting
454 morphogen gradients may support alternative modes of tissue organization. In systems
455 containing transit-amplifying populations, differentiation programs can proceed without
456 immediate cell-cycle exit, expanding intermediate states and producing graded or continuous
457 boundaries[7, 49, 50]. Our findings suggest that the duration and apparent abundance of transitional
458 states are tunable outcomes of morphogen coordination, providing a general framework for how
459 interacting signals regulate the emergence of distinct tissue boundaries tissues (Fig. 7j).
460
461 How SHH signaling elevates Wnt activity is unlikely to involve direct transcriptional activation of
462 Wnt target genes by GLI factors. Instead, our data indicate that elevated Wnt activity is
463 associated with loss of GLI3 chromatin occupancy at loci involved in cell-cycle regulation.
464 Although GLI3 eviction from chromatin does not induce large-scale chromatin architectural
465 reorganization, it coincides with SHH-dependent activation of differentiation genes, suggesting
466 that chromatin-level cross-regulation between Wnt and SHH pathways synchronizes cell-cycle
467 exit with molecular differentiation.
468
469 At the tissue level, this SHH-dependent enhancement of Wnt responsiveness shapes how
470 transitions unfold in space and time. Prior to SHH signaling, dermal cells occupy positions along
471 a Wnt-defined continuum, reflecting differences in transcriptional state. These differences
472 encode competence – how rapidly and synchronously cells traverse the transition once SHH is
473 engaged rather than pre-specified fates. Cells with higher Wnt activity reach cell-cycle exit more

474 rapidly upon SHH activation, whereas cells with lower Wnt activity transition more slowly,
475 expanding intermediate states. In this view, SHH synchronizes progression across a pre-
476 patterned landscape, compressing developmental time locally and producing sharp boundaries
477 without altering the sequence of states traversed.
478
479 Finally, by focusing on an early dermal transition, this work establishes a tractable mammalian
480 system for investigating how interacting morphogen gradients regulate the timing of concurrent
481 biological processes. Integrating *in vivo* genetics with trajectory-based analysis enables
482 resolution of overlapping differentiation programs that are otherwise difficult to detect, revealing
483 how dynamic signaling interactions shape discrete cell-state transitions[34].

484 **Methods**

485 Tamoxifen induction of mice

486 Embryos were staged as days post coitum, with embryonic day E0.5 considered as noon of the
487 day a vaginal plug was detected after overnight mating. Pregnant dams were given one dose of
488 Tamoxifen dissolved in corn oil (20mg/ml, Sigma) at 40-60 µg/gm body weight by oral gavage at
489 E11.5 as indicated.

490 Mice details

491 *Axin2CreER* [51] mice were bred to *Rosa-LSLSmoM2YFP* [52], *β-catenin*$^{fl(Ex3/+}$ [53] and *Gli3*$^{fl/fl}$ [54]
492 mice. *K14Cre* [55] mice were bred to *Shh* Overexpressor (Wang et al. 2010) and *Wntless*$^{fl/fl}$[56]mice.
493 *Rosa-Flag-Gli3YFP* [39] mice were bred to *Axin2CreER* and *β-catenin*$^{fl(Ex3/+}$ mice to enable
494 detection of GLI3-Flag using CUT&RUN. *R26Fucci2aR* [57] reporter mice were used to visualize
495 cell cycle phase. *PDGFRaH2BGFP*[45] mice were used culture embryonic dermal cells.
496 *Sox2eGFP*[58] mice were used to visualize DC cells in embryonic skin whole mounts. A random
497 population of both male and female mice were used for all experiments. All procedures involving
498 animal subjects were performed under the approval of the Institutional Animal Care and Use
499 Committee of the Yale School of Medicine.

500 EdU Incorporation Assay

501 To assess active proliferation, EdU was administered to pregnant mice intraperitoneally (25
502 µg/gm) and embryos were harvested after 1.5 hour. For pulse-chase experiments, 25 µg/gm
503 EdU was administered to pregnant mice at indicated times and embryos were harvested at later
504 times. EdU incorporation was assessed using the Click-it EdU Imaging kit Alexa 555 or Alexa
505 488 (Life technologies, c10338) according to manufacturer's instructions. Briefly, skin explants
506 were treated with a mixture of 1X Click-iT reaction buffer, $CuSO_4$, Alexa Fluor azide dye and 1X
507 reaction buffer additive, all provided in the Click-it EdU Imaging Kit, for 30 minutes at RT before
508 washing in PBS.

509 Histology

510 10% formalin-fixed paraffin embedded (FFPE) whole embryos were used for histological
511 analysis. FFPE embryos were sectioned at 10 µm thickness for FISH.

512 Whole mount immunofluorescence

513 Dorsolateral skin from embryos were microdissected and placed on nucleopore filters (VWR,
514 WHA 800281) and fixed overnight with 4%PFA at 4° C. Skin explants were blocked for 6 hours
515 in 5% normal donkey serum, 1% bovine serum albumin and 0.5% Triton-X100 at RT. Explants
516 were incubated overnight at 4° C in the following primary antibodies: rabbit anti-Sox2 (1:400,
517 Abcam, ab97959), chicken anti-GFP (1:500, Abcam, ab13970), rabbit anti-RFP (1:500,
518 Rockland, 600-401-379). Explants were then washed in 0.2% Tween20/PBS for 4-6 hours on a
519 rotator and then incubated with the following secondary antibodies: Alexa Fluor 568-donkey
520 anti-rabbit (1:200, Invitrogen, A10042), Alexa Fluor 488-donkey anti-rabbit (1:200, Invitrogen,
521 A21206), Alexa Fluor 488-goat anti-chicken (1:200, Invitrogen, A11039) overnight at RT.
522 Washes were carried out for 6 hours with 0.2% Tween20/PBS. Hoechst (1:750 in PBS) was
523 used for 45 min before mounting on slides with SlowFade Gold Antifade Mountant (Invitrogen,
524 S36936).

525 *In-situ* hybridization

526 The RNAscope Multiplex Fluorescent Detection Kit v2 (ACDBio, 323110) was used for single-
527 molecule fluorescence in situ hybridization (FISH) according to the manufacturer's protocol.
528 Briefly, sections were deparaffinized and permeabilized with hydrogen peroxide followed by
529 antigen retrieval and protease treatment before probe hybridization. After hybridization,
530 amplification and probe detection were done using the Amp 1–3 reagents. Probe channels were
531 targeted using the provided HRP-C1-3 reagents and tyramide signal amplification VIVID
532 fluorophores—650 and 570 (ACD biotechne, 323271). EdU staining was done using the Click-it
533 EdU Imaging Kit Alexa 488 (Life Technologies, c10338) according to the manufacturer's
534 instructions. Nuclear counter-stain was done using Hoechst 33342 (Invitrogen, H3570) before
535 mounting with SlowFade Mountant. RNA scope probes used (ACDBio)—Mm-Lef1 (441861),
536 Mm-Ptch1 (402811), Mm-Dkk1 (402521), Mm-Sox2 (401041), Mm-Gal (400961), Mm-Gli3
537 (400961) and Mm-Trp53inp1 (1161531).

538 Microscopy

539 FISH paraffin-embedded images were acquired using the Leica Stellaris 8 DMi8 confocal
540 microscope with a ×40 oil immersion (Numerical Aperture 1.3) objective lens, scanned at 5 μm
541 thickness, 1, 024 × 1, 024 pixel width, 400Hz. Whole mount explants were imaged in 3
542 dimensions using the LaVision TriM Scope II (LaVision Biotec) microscope equipped with a
543 Chameleon Vision II (Coherent) two-photon laser (810 -1000 nm) to acquire *z*-stack images
544 ranging from 50-120 μm (2 μm serial optical sections) using a 20X water immersion lens (NA
545 1.0; Olympus), scanned with a field of view of 0.3–0.5 mm^2 at 800 Hz.

546 Single-cell dissociation

547 Embryonic dorsolateral/flank skin was micro-dissected and pooled after genotyping (3 embryos
548 per condition) and dissociated into a single-cell suspension using 0.25% trypsin (Gibco, Life
549 Technologies) for 14 minutes at 37° C. Single-cell suspensions were then stained with DAPI
550 (Fisher Scientific, NBP2-31156) just prior to fluorescence-activated cell sorting.

551 Fluorescence-activated cell sorting

552 DAPI-excluded live skin cells were sorted on a BD FACS Aria II (Biosciences) sorter with a 100
553 μm nozzle. Cells were sorted in bulk and submitted for 10X Genomics library preparation at
554 0.75-1.0x10^6/mL concentration in 4% FCS/PBS solution.

555 Single-cell RNA sequencing and library preparation

556 Chromium Single cell 3' Library and Gel Bead Kit v2 Chromium Single Cell 3′ Library & Gel
557 Bead Kit v2 (PN-120237), Chromium Single Cell 3′ Chip kit v2 (PN-120236) and Chromium i7
558 Multiplex Kit (PN-120262) were used according to the manufacturer's instructions in the
559 Chromium Single Cell 3′ Reagents Kits V2 User Guide. After cDNA libraries were created, they
560 were subjected to Novaseq 6000 (Illumina) sequencing.

561 10X scRNA-seq data pipeline to matrix

562 The transcriptomes of live single cells from E13.5 or E14.5 mouse skin samples under different
563 biological conditions were sequenced. Raw 10X sequencing data was processed into a matrix
564 employing the standard 10X CellRanger pipeline. Briefly, base call files were fastq format which
565 were aligned to the mm10 reference genome followed by nUMI and barcode counting,
566 constructing the nUMI count matrices. nUMI matrices were filtered, centered and normalized

using Seurat@1. Briefly, for each original run condition (e.g., E13.5 wildtype), cells with > 1,000 detected genes, mitochondrial content < 25%, and ribosomal content > 5% (calculated via PercentageFeatureSet in Seurat) were retained. Doublets were identified and removed using scDblFinder@2. Data were then log-normalized by total UMI count.

Principal Component Calculation and UMAP Visualization

Principal components were computed using Seurat's RunPCA on the top 2,000 variable genes. The number of PCs retained was determined from the elbow plot@7, and used for downstream analysis, including dimensionality reduction for visualization and clustering.

Cell type specification

For each original run, UMAP was performed on log-normalized, centered, and scaled UMI count matrices using the retained PCs. Unsupervised clustering was then conducted using Seurat's FindClusters function with a resolution of 0.5. Clusters expressing Col1a1 were defined as dermal, while clusters expressing Lef1 or Dkk1 were defined as upper-dermal.

Gene trajectory inference

We applied GeneTrajectory@3 to each sample to identify multiple, independent gene dynamic processes. For each sample, we followed the recommended guidelines. We selected the top 2,000 highly variable genes (identified using Seurat's FindVariableFeatures) that were expressed in >1% and <50% of cells as input. The top 20PCs were used to compute a diffusion map, and the top 10 diffusion components were used to construct a cell k-nearest neighbor graph (k = 10).

The number of gene trajectories and the time steps for gene inclusion within each trajectory were determined interactively by inspecting the top three or more gene embeddings. For the samples analyzed in this study, we identified the following gene trajectories and associated time steps (t):

- E14.5 wild type: 3 trajectories (t = 13, 10, 5)
- E13.5 SmoM2: 4 trajectories (t = 1, 3, 2, 1); control: 3 trajectories (t = 3, 2, 2)
- E13.5 TG: 3 trajectories (t = 6, 3, 3); control: 3 trajectories (t = 5, 3, 3)
- E13.5 EX3: 4 trajectories (t = 3, 3, 2, 2); control: 3 trajectories (t = 1, 3, 3)

595 • E13.5 Gli3-KO: 4 trajectories (t = 8, 7, 6, 1); control: 3 trajectories (t = 4, 3, 1)

596 Gene bins and cell stages

597 Following GeneTrajectory guidelines, each trajectory from mutant samples was divided into 5 or
598 6 gene bins. For each bin, a gene bin score was computed for both mutant and control samples
599 to compare gene expression dynamics across the cell embedding. Cell involved in each
600 trajectory were stratified into the same number of stages, based on whether they expressed
601 more than 50% of the genes in the corresponding gene bin. Cells assigned to multiple stages
602 were resolved by assigning them to the stage closer to the terminal end of the trajectory (i.e.,
603 farther from the branching point).

604 Exit GT Score

605 Exit GT scores for each sample were calculated using Seurat's AddModuleScore, based on all
606 genes from the exit gene trajectory identified in E13.5 SmoM2.

607 Pathway enrichment analysis

608 Reactome pathway enrichment analysis was performed using ReactomePA@4, with pathways
609 showing $p < 0.05$ considered significantly enriched.

610 Cell cycle estimation of scRNA-seq data

611 We employed Seurat's cell cycle scoring [59]. Briefly, averaged relative expression of those cell
612 cycle related genes were used to calculate G2/M and S scores, which were used for binning
613 cells into G2/M, S and G1/G0 bins.

614 Data merge and normalization

615 For comparative analysis, we merged upper-dermal cell matrices from each pair of conditions
616 separately (i.e. E13.5 control and Gli3-KO), followed by standard preprocessing and
617 normalization using the workflow provided by Seurat.

618 Differential abundance and Differential gene expression analysis

619 Differential abundant cells were identified using DA-seq@6, with a DA score threshold > 0.8.
620 Differential gene expression analysis between DA cells from E13.5 Gli3-KO and all other upper-
621 dermal cells from both E13.5 Gli3-KO and control was performed using Seurat's FindMarkers

622 without prefiltering. Significant DEGs for visualization were defined using a combined threshold
623 of padj < 1e-5 and log2FC > 0.23.
624 Integrated snATAC+RNA-seq Multi-omic Analysis
625 Single-cell RNA-seq (scRNA-seq) and single-cell ATAC-seq (scATAC-seq) data from E14.5
626 K14Cre;SHH$^{fl/fl}$ and paired control embryonic skin were processed and integrated using the
627 Seurat and Signac packages in R. The scRNA-seq data was normalized using SCTransform.
628 For the scATAC-seq component, dimensionality reduction was performed using Latent
629 Semantic Indexing (LSI). To integrate the modalities, we applied Weighted Nearest Neighbor
630 (WNN) analysis, constructing a joint neighbor graph that represents the weighted combination of
631 RNA and ATAC modalities. A joint UMAP was generated from the WNN graph for visualization.
632 Transcription factor motif accessibilities were calculated using chromVAR.
633
634 <u>CUT&RUN experiments</u>
635 CUT&RUN was performed with the Epicypher CUTANA™ ChIC/CUT&RUN Kit (14-1048)
636 according to the manufacturer's specifications with the following conditions: 500,000 cells per
637 sample were prepared first and nuclei were extracted according to the Epicypher CUT&RUN
638 Manual Appendix. Nuclei were incubated with activated ConA beads. The following antibodies
639 (0.5 ug of antibody per reaction) were used:
640 IgG Control antibody: CUTANA™ Kit Rabbit IgG CUT&RUN Negative Control Antibody,
641 EpiCypher Rabbit anti-H3K27Ac antibody, Millipore Mouse anti-Flag antibody, Antibodies-online
642 Rabbit anti-CTNNB1 antibody.
643 Libraries were prepared using the Epicypher CUTANA™ CUT&RUN Library Prep Kit (14-1002)
644 according to the manufacturer's specifications. Library quality was analyzed using Agilent
645 Tapestation D1000 High Sensitivity Tapes (#5067-5584). Sequencing was performed with 5
646 million 150bp paired-end reads per sample on an Illumina NovaSeq 6000.
647 <u>CUT&RUN data analysis</u>
648 CUT&RUN reads were analyzed for quality using FastQC
649 (https://www.bioinformatics.babraham.ac.uk/projects/fastqc/) and adaptors trimmed using

650 Trimmomatic. Reads were then aligned to mm9 by Bowtie2 version 2.3.1. SAMTools version
651 1.11 was then used to convert to BAM format, index, isolate uniquely mapped paired reads, and
652 remove duplicates. MACS2 version 2.2.8 was used to call peaks with IgG as input control. Read
653 counts across genomic intervals and peak visualization were performed using deepTools
654 version 3.5 and bigwig files were visualized using the Integrative Genomics Viewer. Deseq2
655 was used to identify differentially bound peaks between conditions, DiffBind used to plot
656 heatmaps of accessible/bound regions and HOMER to identify *de novo* motifs most enriched in
657 the differentially bound regions and annotate associated genes.

658 Micro-C Experiments

659 Micro-C was performed using the Dovetail® Micro-C Kit (Cantata Bio, PN 21006E) according to
660 the manufacturer's protocol using 1 million cells per reaction. E13.5 mouse dorsolateral dermis
661 was microdissected, dissociated, and crosslinked with formaldehyde, followed by quenching
662 and nuclei isolation. Chromatin was digested with micrococcal nuclease, end-repaired, and
663 proximity ligated to capture nucleosome-level chromatin contacts. Reverse crosslinking and
664 DNA purification were performed following kit specifications. Libraries were prepared using the
665 Dovetail® Library Module for Illumina (PN 25004E) and indexed with the manufacturer-provided
666 i5/i7 primer sets. Library quality and fragment size distribution were assessed using the Agilent
667 TapeStation High Sensitivity D5000 assay (Agilent #5067-5592**, #**5067-5593**, #**5067-5594).
668 Final libraries were sequenced on an Illumina NovaSeq 6000 platform to a depth of 300 million
669 150-bp paired-end reads per biological replicate.

670 Micro-C data analysis

671 Micro-C reads were aligned to the *mm10* genome using BWA-MEM with proximity-ligation–
672 optimized settings, and ligation junctions were identified, sorted, and deduplicated using the
673 Pairtools pipeline to generate uniquely mapped, non-duplicate valid pairs. Valid pairs were
674 converted into 5-kb contact matrices using cooler (v0.10.4**),** balanced by iterative correction,
675 and aggregated into multi-resolution .mcool files for downstream analysis. Chromatin loops
676 were identified using Mustache (v1.2.0), a multi-scale loop-calling algorithm that applies scale-
677 space representation to detect interaction peaks across resolutions in high-resolution Micro-C

678 maps. Loop anchors were intersected with CUT&RUN peaks using Bedtools (v2.27.1) to
679 annotate interactions. Genome-wide A/B chromatin compartments were computed at 40-kb
680 resolution using FAN-C (v0.9.28), which generated Pearson correlation matrices and extracted
681 the first principal component to assign A/B compartment identity. Processed matrices, loops,
682 and eigenvector tracks were visualized using FAN-C.

683 Western blot

684 Cells were lysed in RIPA buffer (Thermo Fisher Scientific, Cat# 89900) supplemented with
685 protease inhibitors (Thermo Fisher Scientific, Cat# 87786) for 30 minutes at 4 °C. The lysates
686 were clarified by centrifugation at 10,000 × g for 20 minutes at 4 °C, and protein concentrations
687 were determined using Bradford Protein Assay Kit (Bio-Rad, Cat# 5000006). Equal amounts of
688 protein (10 µg) were denatured at 95 °C for 5 minutes and loaded onto 4–12% precast
689 polyacrylamide gels (Bio-Rad, Cat# 3450125) for electrophoresis. Proteins were transferred to
690 PVDF membranes (Thermo Fisher Scientific, Cat# IB24001) using an iBlot2 transfer device
691 (Invitrogen, Cat# IB21001). Membranes were blocked with 5% BSA (vol/vol) in 1× TBST
692 (AmericanBio, Cat# AB14330-01000) at room temperature, incubated with primary antibodies
693 overnight at 4 °C, washed three times with TBST for 5 minutes each, incubated with HRP-
694 conjugated secondary antibodies for 1 hour at room temperature, and washed again three times
695 with TBST.

696 Membranes were developed using SuperSignal West Pico PLUS Chemiluminescent Substrate
697 (Thermo Fisher Scientific, Cat# 34577) and imaged on a ChemiDoc imaging system (Bio-Rad).
698 The following antibodies were used: mouse anti-Flag (Millipore, Cat# F1804), rabbit anti-Actin
699 (Cell Signaling Technology, Cat# 4970), HRP-conjugated goat anti-rabbit IgG (Cell Signaling
700 Technology, Cat# 7074), and HRP-conjugated goat anti-mouse IgG (Bio-Rad, Cat# STAR207P,
701 1:10,000).

702 Dermal cell culture

703 E13.5 PDGFRαH2BGFP skin cells were sorted based on their GFP status. GFP+ cells were
704 collected and pelleted (300 × g, 10 min, 4°C), resuspended at 2×10^6 cells/mL in complete
705 growth medium (DMEM + 10% FBS, Penicillin-Streptomycin, and L-Glutamine), and viability

706 was assessed by trypan blue exclusion. Cells were plated at 3×10^6 cells/well in 6-well plates in
707 2 mL total volume. For chemical perturbation assays, cells were mixed 1:1 with a 2× agonist
708 solution. For example, 5 μM CHIR99021 (Sigma, Cat# SML1046) was prepared in DMSO and
709 diluted to a working concentration of 5 μM in culture. Similarly, SAG (Sigma, Cat# SML1314)
710 was prepared as a 50 μM stock and diluted as needed. Media with agonist was used fresh or
711 stored at 4°C for up to two days. Cells were cultured in 48-72 hours. For 3D culture, 3×10^5 cells
712 were seeded onto each well of a μ-slide 8 Well Glass Bottom chamber (ibidi, Cat#80807) which
713 has been precoated by 1.5mg/mL Collagen Type I (Corning, Cat#354236). Collagen Type I was
714 neutralized by manufacture instructions and 200uL was added to each well 1 hour prior to
715 seeding the cells for solidification.

716 Quantitative PCR

717 Total RNA was extracted from cultured cells using the RNeasy Mini Kit (Qiagen, Cat# 74134)
718 according to the manufacturer's protocol. Complementary DNA (cDNA) was synthesized from
719 500 ng–1 μg of total RNA using the SuperScript™ III First-Strand Synthesis System (Invitrogen,
720 Cat# 18080051) with random hexamer primers. Quantitative PCR was performed using the
721 PowerUp™ SYBR™ Green Master Mix (Thermo Fisher Scientific, Cat# 4364344) on a Viia7
722 Real-Time PCR System (Applied Biosystems) in 384-well optical plates. Reactions were run in
723 technical triplicates using gene-specific primers, and threshold cycle (Ct) values were
724 normalized to Gapdh as a housekeeping gene. Relative expression was calculated using the
725 ΔΔCt method.

726 3D culture immunofluorescence

727 Cultured cells with collagen were fixed for 25 minutes with 4%PFA at room temperature. They
728 were blocked for 2-4 hours in 5% normal donkey serum, 1% bovine serum albumin and 0.2%
729 Triton-X100 at RT. Cells were incubated overnight at 4° C in the following primary antibodies:
730 rat anti-Ki67 (1:200, Invitrogen, 14-5698-82), rabbit anti-Robo2 (1:200, Cell signaling, 45568).
731 Cells were then washed in 1x PBS for 4-6 hours and then incubated with the following
732 secondary antibodies: Alexa Fluor 568-goat anti-rat (1:200, Invitrogen, A11077) and Alexa Fluor
733 647-donkey anti-rabbit (1:200, Invitrogen, A31573) overnight at 4° C. Washes were carried out

734 for 6 hours with 1x PBS. Hoechst (1:750 in PBS) was used for 45 min before washing in 1x
735 PBS.

736 Image analysis

737 Raw image stacks acquired from whole-mount explants were imported into Fiji or Adobe
738 Photoshop for analysis. ggplot2 and cowplot R libraries were used for graphical representation
739 of the scRNA-seq data. Diffusion maps were generated as described above.

740 Quantification

741 For quantification of DC density, 3-dimensional whole-mount tiled mosaics of skin explants with
742 a 1000 x 1000 μm field of view and a z-depth of 60-100 μm were used for n=3-4 embryos. For
743 volumetric quantification of DC cell number, EdU+ or Tom+ percentage of DC or UD, 3-
744 dimensional whole mount mosaics stained with Sox2 and EdU or RFP were used to manually
745 count positive cells, using ImageJ (Fiji) software using planar (XY) and orthogonal (YZ, XZ)
746 views. For volumetric quantification of cell cycle phases, 3-dimensional whole mount mosaics
747 stained with markers for G0/G1 cells (based on Fucci2 reporter) were done manually by
748 counting nuclear positive cells using ImageJ (Fiji) software. For quantification of upper dermal
749 cells, a distance of 10 um below the epidermis was considered upper dermis. For quantification
750 of the peri-DC region by whole-mount, cells two cell layers out from the Sox2+ DC were
751 counted. For quantification based on FISH, cells with 4-5 dots were considered positive
752 (according to the RNAScope manufacturer's instructions) and sections from a total of n=4
753 different embryos were examined. To measure RNA expression levels, H-scores were
754 calculated according to ACDBio manufacturer's instructions: a cell with 0 dot is scored 0, 1-3
755 dots score 1, 4-9 dots score 2, 10-15 dots and/or less than 10% clustered dots score 3, and
756 more than 15 dots and/or more than 10% clustered dots score 4; then the final H-score of a
757 given cell type A is calculated by summing the (% cells scored B within all cells in A)*B for score
758 B in 0-4. For quantification of upper dermal cells, a distance of 10-20 μm below the epidermis
759 was considered as upper dermis. For quantification of cells in the peri-DC region *Dkk1+Sox2-*
760 was considered.

761 Statistical analysis

762 All statistical values are expressed as mean ± SEM. An unpaired Student's *t*-test was used to
763 analyze data sets with two groups and *P <0.05 to, **P<0.01, ***P< 0.001 and ****P<0.00001
764 indicated a significant difference. When comparing more than two groups, P values were
765 determined by one-way ANOVA with Tukey's HSD test performed as the post hoc analysis.
766 Statistical calculations were performed using Prism software package (GraphPad). For
767 categorical data, a chi-square test was employed to estimate a P value.
768 No statistical methods were used to predetermine sample size. The experiments were not
769 randomized. The investigators were not blinded to allocation during experiments and outcome
770 assessment.

771 **Data and Code Availability**

772 Genomic datasets used in this study will be deposited in NCBI Gene Expression Omnibus
773 database and made publicly available as of the date of publication or with a token upon request.

774

775 **References**

776 1. Wolpert, L. Positional information and the spatial pattern of cellular differentiation. *J*
777 *Theor Biol* **25**, 1-47 (1969).
778 2. Benzinger, D. & Briscoe, J. Investigating morphogen and patterning dynamics with
779 optogenetic control of morphogen production. *Dev Cell* **60**, 3421-3430 e3426 (2025).
780 3. Driever, W. & Nusslein-Volhard, C. The bicoid protein determines position in the
781 Drosophila embryo in a concentration-dependent manner. *Cell* **54**, 95-104 (1988).
782 4. Greenfeld, H., Lin, J. & Mullins, M.C. The BMP signaling gradient is interpreted through
783 concentration thresholds in dorsal-ventral axial patterning. *PLoS Biol* **19**, e3001059
784 (2021).
785 5. Roelink, H. *et al.* Floor plate and motor neuron induction by different concentrations of
786 the amino-terminal cleavage product of sonic hedgehog autoproteolysis. *Cell* **81**, 445-
787 455 (1995).
788 6. Teague, S. *et al.* Time-integrated BMP signaling determines fate in a stem cell model for
789 early human development. *Nat Commun* **15**, 1471 (2024).

790 7. Morita, R. *et al.* Tracing the origin of hair follicle stem cells. *Nature* **594**, 547-552 (2021).
791 8. Ouspenskaia, T., Matos, I., Mertz, A.F., Fiore, V.F. & Fuchs, E. WNT-SHH Antagonism
792 Specifies and Expands Stem Cells prior to Niche Formation. *Cell* **164**, 156-169 (2016).
793 9. Rompolas, P. *et al.* Live imaging of stem cell and progeny behaviour in physiological
794 hair-follicle regeneration. *Nature* **487**, 496-499 (2012).
795 10. Zhang, C. *et al.* Escape of hair follicle stem cells causes stem cell exhaustion during
796 aging. *Nat Aging* **1**, 889-903 (2021).
797 11. Leybova, L. *et al.* Radially patterned morphogenesis of murine hair follicle placodes
798 ensures robust epithelial budding. *Dev Cell* **59**, 3272-3289 e3275 (2024).
799 12. Driskell, R.R. *et al.* Distinct fibroblast lineages determine dermal architecture in skin
800 development and repair. *Nature* **504**, 277-281 (2013).
801 13. Myung, P., Andl, T. & Atit, R. The origins of skin diversity: lessons from dermal
802 fibroblasts. *Development* **149** (2022).
803 14. Chuong, C.M., Widelitz, R.B., Ting-Berreth, S. & Jiang, T.X. Early events during avian
804 skin appendage regeneration: dependence on epithelial-mesenchymal interaction and
805 order of molecular reappearance. *J Invest Dermatol* **107**, 639-646 (1996).
806 15. Chase, H.B., Rauch, R. & Smith, V.W. Critical stages of hair development and
807 pigmentation in the mouse. *Physiol Zool* **24**, 1-8 (1951).
808 16. Gupta, K. *et al.* Single-Cell Analysis Reveals a Hair Follicle Dermal Niche Molecular
809 Differentiation Trajectory that Begins Prior to Morphogenesis. *Dev Cell* **48**, 17-31 e16
810 (2019).
811 17. Hardy, M.H. The secret life of the hair follicle. *Trends Genet* **8**, 55-61 (1992).
812 18. Millar, S.E. *et al.* WNT signaling in the control of hair growth and structure. *Dev Biol* **207**,
813 133-149 (1999).
814 19. Paus, R. *et al.* A comprehensive guide for the recognition and classification of distinct
815 stages of hair follicle morphogenesis. *J Invest Dermatol* **113**, 523-532 (1999).
816 20. Saxena, N., Mok, K.W. & Rendl, M. An updated classification of hair follicle
817 morphogenesis. *Exp Dermatol* **28**, 332-344 (2019).

818 21. Woo, W.M., Zhen, H.H. & Oro, A.E. Shh maintains dermal papilla identity and hair
819 morphogenesis via a Noggin-Shh regulatory loop. *Genes Dev* **26**, 1235-1246 (2012).
820 22. Chen, D., Jarrell, A., Guo, C., Lang, R. & Atit, R. Dermal beta-catenin activity in
821 response to epidermal Wnt ligands is required for fibroblast proliferation and hair follicle
822 initiation. *Development* **139**, 1522-1533 (2012).
823 23. Noramly, S., Freeman, A. & Morgan, B.A. beta-catenin signaling can initiate feather bud
824 development. *Development* **126**, 3509-3521 (1999).
825 24. Chiang, C. *et al.* Essential role for Sonic hedgehog during hair follicle morphogenesis.
826 *Dev Biol* **205**, 1-9 (1999).
827 25. St-Jacques, B. *et al.* Sonic hedgehog signaling is essential for hair development. *Curr*
828 *Biol* **8**, 1058-1068 (1998).
829 26. Gritli-Linde, A. *et al.* Abnormal hair development and apparent follicular transformation to
830 mammary gland in the absence of hedgehog signaling. *Dev Cell* **12**, 99-112 (2007).
831 27. Qu, R. *et al.* Decomposing a deterministic path to mesenchymal niche formation by two
832 intersecting morphogen gradients. *Dev Cell* **57**, 1053-1067 e1055 (2022).
833 28. Xu, Z. *et al.* Embryonic attenuated Wnt/beta-catenin signaling defines niche location and
834 long-term stem cell fate in hair follicle. *Elife* **4**, e10567 (2015).
835 29. Ben-Zvi, D., Shilo, B.Z., Fainsod, A. & Barkai, N. Scaling of the BMP activation gradient
836 in Xenopus embryos. *Nature* **453**, 1205-1211 (2008).
837 30. Dekanty, A. & Milan, M. The interplay between morphogens and tissue growth. *EMBO*
838 *Rep* **12**, 1003-1010 (2011).
839 31. Gregor, T., Wieschaus, E.F., McGregor, A.P., Bialek, W. & Tank, D.W. Stability and
840 nuclear dynamics of the bicoid morphogen gradient. *Cell* **130**, 141-152 (2007).
841 32. Kicheva, A., Bollenbach, T., Wartlick, O., Julicher, F. & Gonzalez-Gaitan, M.
842 Investigating the principles of morphogen gradient formation: from tissues to cells. *Curr*
843 *Opin Genet Dev* **22**, 527-532 (2012).
844 33. Lander, A.D., Nie, Q. & Wan, F.Y. Do morphogen gradients arise by diffusion? *Dev Cell*
845 **2**, 785-796 (2002).

846 34. Qu, R. *et al.* Gene trajectory inference for single-cell data by optimal transport metrics.
847 *Nat Biotechnol* (2024).
848 35. Biggs, L.C. *et al.* Hair follicle dermal condensation forms via Fgf20 primed cell cycle exit,
849 cell motility, and aggregation. *Elife* **7** (2018).
850 36. Zhang, Y. *et al.* Reciprocal requirements for EDA/EDAR/NF-kappaB and Wnt/beta-
851 catenin signaling pathways in hair follicle induction. *Dev Cell* **17**, 49-61 (2009).
852 37. Fu, J. & Hsu, W. Epidermal Wnt controls hair follicle induction by orchestrating dynamic
853 signaling crosstalk between the epidermis and dermis. *J Invest Dermatol* **133**, 890-898
854 (2013).
855 38. Alvarez-Medina, R., Cayuso, J., Okubo, T., Takada, S. & Marti, E. Wnt canonical
856 pathway restricts graded Shh/Gli patterning activity through the regulation of Gli3
857 expression. *Development* **135**, 237-247 (2008).
858 39. Vokes, S.A., Ji, H., Wong, W.H. & McMahon, A.P. A genome-scale analysis of the cis-
859 regulatory circuitry underlying sonic hedgehog-mediated patterning of the mammalian
860 limb. *Genes Dev* **22**, 2651-2663 (2008).
861 40. te Welscher, P. *et al.* Progression of vertebrate limb development through SHH-
862 mediated counteraction of GLI3. *Science* **298**, 827-830 (2002).
863 41. Heinz, S. *et al.* Simple combinations of lineage-determining transcription factors prime
864 cis-regulatory elements required for macrophage and B cell identities. *Mol Cell* **38**, 576-
865 589 (2010).
866 42. Lex, R.K. *et al.* GLI transcriptional repression is inert prior to Hedgehog pathway
867 activation. *Nat Commun* **13**, 808 (2022).
868 43. Phan, Q.M. *et al.* Lef1 expression in fibroblasts maintains developmental potential in
869 adult skin to regenerate wounds. *Elife* **9** (2020).
870 44. Reddy, S. *et al.* Characterization of Wnt gene expression in developing and postnatal
871 hair follicles and identification of Wnt5a as a target of Sonic hedgehog in hair follicle
872 morphogenesis. *Mech Dev* **107**, 69-82 (2001).

873 45. Hamilton, T.G., Klinghoffer, R.A., Corrin, P.D. & Soriano, P. Evolutionary divergence of
874 platelet-derived growth factor alpha receptor signaling mechanisms. *Mol Cell Biol* **23**,
875 4013-4025 (2003).
876 46. Guzman-Palma, P. *et al.* Slit/Robo Signaling Regulates Multiple Stages of the
877 Development of the Drosophila Motion Detection System. *Front Cell Dev Biol* **9**, 612645
878 (2021).
879 47. Goncalves, A.N., Correia-Pinto, J. & Nogueira-Silva, C. ROBO2 signaling in lung
880 development regulates SOX2/SOX9 balance, branching morphogenesis and is
881 dysregulated in nitrofen-induced congenital diaphragmatic hernia. *Respir Res* **21**, 302
882 (2020).
883 48. Reyes, R., Lander, A.D. & Nahmad, M. Dynamic readout of the Hh gradient in the
884 Drosophila wing disc reveals pattern-specific tradeoffs between robustness and
885 precision. *Elife* **13** (2024).
886 49. Sun, Q. *et al.* Dedifferentiation maintains melanocyte stem cells in a dynamic niche.
887 *Nature* **616**, 774-782 (2023).
888 50. Myung, P. & Ito, M. Dissecting the bulge in hair regeneration. *J Clin Invest* **122**, 448-454
889 (2012).
890 51. van Amerongen, R., Bowman, A.N. & Nusse, R. Developmental stage and time dictate
891 the fate of Wnt/beta-catenin-responsive stem cells in the mammary gland. *Cell Stem Cell*
892 **11**, 387-400 (2012).
893 52. Jeong, J., Mao, J., Tenzen, T., Kottmann, A.H. & McMahon, A.P. Hedgehog signaling in
894 the neural crest cells regulates the patterning and growth of facial primordia. *Genes Dev*
895 **18**, 937-951 (2004).
896 53. Harada, N. *et al.* Intestinal polyposis in mice with a dominant stable mutation of the beta-
897 catenin gene. *EMBO J* **18**, 5931-5942 (1999).
898 54. Blaess, S., Stephen, D. & Joyner, A.L. Gli3 coordinates three-dimensional patterning
899 and growth of the tectum and cerebellum by integrating Shh and Fgf8 signaling.
900 *Development* **135**, 2093-2103 (2008).

901 55. Dassule, H.R., Lewis, P., Bei, M., Maas, R. & McMahon, A.P. Sonic hedgehog regulates
902 growth and morphogenesis of the tooth. *Development* **127**, 4775-4785 (2000).
903 56. Carpenter, A.C., Rao, S., Wells, J.M., Campbell, K. & Lang, R.A. Generation of mice
904 with a conditional null allele for Wntless. *Genesis* **48**, 554-558 (2010).
905 57. Abe, T. *et al.* Visualization of cell cycle in mouse embryos with Fucci2 reporter directed
906 by Rosa26 promoter. *Development* **140**, 237-246 (2013).
907 58. Arnold, K. *et al.* Sox2(+) adult stem and progenitor cells are important for tissue
908 regeneration and survival of mice. *Cell Stem Cell* **9**, 317-329 (2011).
909 59. Nestorowa, S. *et al.* A single-cell resolution map of mouse hematopoietic stem and
910 progenitor cell differentiation. *Blood* **128**, e20-31 (2016).
911

912 **Acknowledgements**

913 We thank D. Gay, M. Ito, J. Levinsohn, and R. Atit for review and discussion of this manuscript.
914 We thank J. Wang and K. Sumigray for generously sharing their Stellaris equipment and help
915 with imaging troubleshooting. Inducible SHH ligand transgenic mice were kindly provided by
916 David Wang. This work was supported by National Institutes of Health grants R01AR076420
917 (P.M.) and LEO Foundation LF-OC-23-001347 (P.M.).
918

919 **Author Contributions**

920 Conceptualization, P.M., Y.K., R.L., Y.J., S.P.; Methodology, P.M., R.L., Y.K., Y.J., S.P., E.B.,
921 S.V., H.L.; Software, R.L., Y.K.; Resources, M.T., K.P.; Investigation, P.M., R.L., Y.J., S.P. H.L,
922 E.B., S.V.; Writing – Original Draft, P.M.; Writing – Review & Editing, P.M., R.L., Y.J., S.P., T.X.,
923 R.D., Y.K., C.L., S.L., E.B.; Supervision, P.M., Y.K.; Funding Acquisition, P.M.
924

925 **Competing Interests**

926 The authors declare no competing interests.
927

928 **Main Figure Legends:**

929 **Fig. 1: Cell-cycle exit and molecular differentiation are tightly coupled during dermal**
930 **condensate formation**

931 **a,** Left, illustration of the French flag problem with stripes representing distinct cell-type readouts
932 positioned relative to a fixed morphogen source. Classical models propose that threshold
933 concentrations of morphogen specify different cell-types with sharp borders. Right, schematic
934 depiction of cellular responses to a linear morphogen gradient, illustrating either linear
935 responses or non-linear transitions across morphogen levels. This contrasts static spatial
936 threshold interpretations with a dynamic view in which cells traverse morphogen levels during
937 fate transitions. **b,** FISH images of E14.5 mouse skin showing *Sox2*+ DCs form by E14.5, which
938 lack EdU copositivity; quantification of %EdU by cell-type (UD, upper interfollicular dermis)
939 (n=10). **c,** FISH image showing peri-DC (*Dkk1*+) cells adjacent to *Sox2*+ with *Cdkn1a* enriched
940 at the DC boundary; (n=10). **d,** E14.5 skin stained for *Lef1* and *Ptch1* with transcripts quantified
941 by spatial regions (LD, lower dermis) or %EdU+ by *Lef1* bin (n=5). **e,** Schematic summarizing
942 dermal cell states with respect to spatial position and relative Wnt and SHH activity levels. DCs
943 arise within regions of overlapping Wnt and SHH activity, where cell-cycle exit and DC gene
944 expression occur within a narrow temporal window. Data as mean± SEM; *P<0.05, **P<0.01,
945 ***P<0.001, ****P<0.0001, one-way ANOVA; ns, not significant. Scale bars=50 μm.
946

948 **Fig. 2: High Wnt activity induces cell-cycle exit independently of SHH signaling**

949 **a,** Experimental setup in which β–catenin was constitutively activated in the dermis prior to DC
950 formation (tamoxifen E11.5). **b,** UMAPs colored by indicated genes or cell cycle (CC) phase for
951 E13.5 Actβcat mutant or paired control dermal scRNA-seq data (n=2). **c,** FISH showing E13.5
952 *Lef1*, *Cdkn1a*, EdU (left) and quantification of UD *Cdkn1a* transcripts (H-score) or %EdU of
953 *Cdkn1a* (*p21*)+ or *p21*- cells in Actβcat UD vs. control UD (*p21*-) (n=3). **d,** FISH showing E14.5
954 *Sox2*, *Cdkn1a*, EdU (left) and quantification of %EdU+ cells in control or Actβcat *Cdkn1a*+ cells
955 (almost all *Cdkn1a*+ cells co-express *Sox2* in control, n=5). **e,** E14.5 *Lef1*, *Ptch1*, *Sox2* FISH-
956 stained sections (left) and quantification of *Ptch1* levels in Actβcat by cell type. **f,** Illustration
957 showing that activated βcatenin (elevated Wnt activity) induces cell-cycle exit at E13.5 in the
958 absence of SHH. At later stages, DC gene expression is restricted to cells experiencing high
959 SHH activity with high Wnt activity. Data as mean± SEM; *P<0.05, **P<0.01, ***P<0.001,
960 ****P<0.0001, one-way ANOVA; ns, not significant. Scale bars=50 μm.

961
962
963
964
965

966 **Fig. 3: SHH signaling cell-autonomously elevates Wnt activity in association with cell-**
967 **cycle exit**
968 **a,** Experimental setup showing expression of constitutively activated Smoothened in dermal
969 cells prior to DC formation when Wnt activity is low (tamoxifen E11.5). **b,** Whole-mount images
970 of E14.5 ActSMO and control skin stained with EdU and Sox2 with quantification of %EdU+ of
971 Sox2+ cells (n=8). **c,** UMAPs of E13.5 control and ActSMO dermal scRNA-seq data with
972 indicated gene expression; right, quantification of scRNA-seq *Lef1* levels in UD cells. **d,** E13.5
973 control or ActSMO mutant skin stained for *Lef1*, *Ptch1* and *Cdkn1a* with quantification of
974 average *Lef1* expression by *Ptch1* expression status (n=8). **e,** E13.5 skin showing ActSMO
975 boosts *Lef1* gene expression which corresponds with decreased EdU incorporation (%EdU). **f,**
976 Cartoon illustrating that high SHH activity cell-autonomously elevates Wnt signaling, and
977 elevated Wnt activity coincides with cell-cycle exit. Data as mean± SEM; *P<0.05, **P<0.01,
978 ***P<0.001, ****P<0.0001, one-way ANOVA. Scale bars, 50 μm.
979

980 **Fig. 4: GeneTrajectory defines transcriptional changes accompanying cell-cycle exit**

981 **a,** GeneTrajectory diffusion map and gene order of E14.5 wildtype DC GT with dermal UMAPs
982 colored by DC GT stages. **b,** *Lef1* and *Ptch1* levels by DC GT stage. **c,** DC gene expression by
983 DC GT stage. Right, G1/G0 fraction by DC GT stage with UMAP of *Cdkn1a* expression or CC
984 phase. **d,** E13.5 ActSMO GT diffusion map. **e,** ActSMO and control dermal UMAPs colored by
985 expression of the mutant New GT stages or CC phase. **f,** Pathway analysis of genes from new
986 mutant GT and UMAPs of control and mutant dermal cells colored by indicated genes. **g,** FISH
987 images of indicated genes in E13.5 control or ActSMO skin with quantification of *Lef1*
988 expression in control E13.5 upper dermal (UD) or E14.5 DC cells vs. E13.5 ActSMO *Trp53inp1*+
989 cells (n=3). **h,** Label transfer of the E13.5 ActSMO new GT onto indicated E13.5 mutant or
990 control dermal populations showing cells that express this similar gene module. **i,** EdU pulse-
991 chase experiments of E13.5-E14.5 ActSMO mutant and corresponding quantification of %EdU
992 of *Trp53inp1*+ cells (n=3). Bottom cartoon illustrating *Trp53inp1*+ cells undergo cell cycle exit as
993 immediately after a division. Data as mean ± SEM, one-way ANOVA. Scale bars, 50 μm.
994

995 **Fig. 5: Loss of GLI3 chromatin binding induces premature cell-cycle exit downstream of**
996 **elevated Wnt signaling**

997 **a,** *Gli3* expression in E13.5 control and Actβcat skin prior to SHH. **b,** Heat map of GLI3 binding
998 at all transcriptional start sites (TSS) in E13.5 control or Actβcat skin. **c,** KEGG pathway analysis
999 of GLI3 unbound regions in the Actβcat mutant. Right, Genome browser tracks showing binding
1000 signal of respective antibodies at indicated genes. **d,** Western blot of cell lysates from control or
1001 Actβcat mutant skin stained with anti-Flag (Gli3) or β-actin (n=3). **e,** FISH of E14.5 control and
1002 Gli3 dermal cKO (tamoxifen E11.5) stained for indicated genes; quantification of DC size and
1003 %EdU of control or Gli3 cKO by cell type (n=3). **f,** FISH of E13.5 control and Gli3 cKO stained
1004 for indicated genes with quantification of transcripts by FISH (n=4). **g,** snATAC+RNA-seq
1005 UMAPs of co-embedded E14.5 control and epidermal SHH cKO showing either gene
1006 expression or GLI motif accessibility. **h,** GT diffusion map of E13.5 Gli3 cKO dermal cells,
1007 showing an Exit GT. UMAPs of control or Gli3 cKO colored by Exit GT bins, indicated genes or
1008 cell-cycle phase. **i,** Label transfer of E13.5 ActSMO Exit GT onto Gli3 cKO or control scRNA-seq
1009 data showing a shared Exit gene GT. **j,** Elevated Wnt activity reduces GLI3 chromatin
1010 occupancy, derepressing genes that mediate cell-cycle exit, but not DC differentiation. Here,
1011 canonical SHH target genes and DC differentiation genes remain inactive in the absence of
1012 SHH signaling. Upon co-activation of Wnt and SHH, canonical SHH targets and DC genes are
1013 induced. Data as mean± SEM; *P<0.05, **P<0.01, ***P<0.001, ****P<0.0001, one-way ANOVA;
1014 ns, not significant; scale bars, 50 μm.
1015

1016 **Fig. 6: Uniformly high SHH activity induces dermal condensate gene expression across**
1017 **the Wnt gradient**

1018 **a,** E13.5 ActSMO dermal GT diffusion map. **b,** Gene order (top) of ActSMO DC GT, showing DC
1019 genes expressed across the trajectory; expression of DC GT stages colored onto ActSMO
1020 dermal UMAPs. **c,** Expression levels of DC genes by DC GT stage. **d,** *Lef1* levels by DC GT
1021 stage of ActSMO and control. **e,** Cartoon illustrating that uniform SHH activation permits DC
1022 gene expression across a range of Wnt activity levels, resulting in sequential induction of DC
1023 genes that correlates with *Lef1* levels. Here, DC genes can be expressed in proliferating cells of
1024 lower Wnt activity, expanding intermediate states before coordinated cell-cycle exit is achieved.
1025 The orange/gray bars represent the extent of intermediate DC transcriptional states along the
1026 trajectory and not a direct measure of temporal kinetics.
1027

1028 **Fig. 7: Coordinated Wnt and SHH signaling synchronizes cell-cycle exit and dermal**
1029 **condensate differentiation**

1030 **a,** Experimental design to test whether coordinated Wnt and SHH activity is sufficient to
1031 synchronize cell cycle exit with DC genes by co-expressing Wnt and SHH ligands across the
1032 epidermis at E13.5 (*K14Cre;Lox-STOP-Lox-Shh*; SHH OE). **b,** FISH images of E13.5 control
1033 and mutant showing covarying levels of *Ptch1* and *Lef1* across vertical dermal layers in the SHH
1034 OE mutant and elevated *Lef1* levels in layers where *Ptch1* is concurrently activated. **c,** E14.5
1035 control and SHH OE with spatial partitioning of cells by cell type genes and *Cdkn1a* coinciding
1036 with *Sox2* expression (n=3). **d,** E13.5 control or SHH OE UMAPs with indicated genes or cell-
1037 cycle phase. **e,** GT diffusion map of E13.5 SHH OE dermal scRNA-seq data. **f,** DC GT gene
1038 order of SHH OE (top) with expression of DC genes and fraction G1/G0 by DC GT stage
1039 (bottom) showing coincident induction of DC genes and cell-cycle exit at the terminal stage.
1040 Right, covarying *Lef1* and *Ptch1* levels by DC GT stage. **g,** Heat map of GLI3 binding at TSS in
1041 E13.5 control versus SHH OE. Genome browser tracks showing reduced GLI3 binding and
1042 active histone marks at *Gli1* and *Ptch1*. **h,** Cartoon showing loss of GLI3 binding upon Wnt and
1043 SHH coactivation with activation of canonical SHH targets. **i,** Confocal images of 3D dermal
1044 cultures stained with Robo2 (DC marker) showing Robo2+ clusters lacking Ki67 in high
1045 CHIR+SAG condition. Right, dermal cluster number in 3D cultures by condition. **j,** Model
1046 illustrating how coordination between Wnt and SHH signaling regulates the timing of cell-cycle
1047 exit and molecular differentiation during the pre-DC-to-DC transition. When morphogen activities
1048 are uncoupled, intermediates states proliferate and persist over a broader temporal and/or
1049 spatial window. Coordinated morphogen dynamics compress the transitional window, yielding
1050 an abrupt cell-state transition. The pink bar in wildtype indicates the spatial field of SHH
1051 activation. The dotted line represents the spatial profile of Wnt activity observed at E13.5 prior to
1052 SHH expression, modeled here as a baseline gradient. Data as mean± SEM; ***P*<0.01,
1053 ****P*<0.001, *****P*<0.0001, one-way ANOVA; ns, not significant; scale bars, 50 μm.

1054
1055

Fig. 1

a **How do sharp cell-type borders form from a smooth morphogen gradient?**

Gradient model for the French Flag Problem

Morphogen concentration

Source

Cell-type Transition

Spatial morphogen gradient

Morphogen activity

Cell-type

Source

Morphogen Activity/ Concentration

C_1

Gradual cell-type Transition

Fuzzy border

Sharp borders by threshold levels of morphogen

Morphogen Concentration

C_1

C_2

Source

Source

Morphogen Activity/ Concentration

C_1

Temporally condensed cell-type Transition

Sharp border

Cells traverse a range of morphogen levels during transition

b

Sox2

EdU

E14.5

Proliferation

% EdU+

60

40

20

0

**** ****

UD

Peri DC (*Dkk1+*)

DC (*Sox2+*)

c

Cdkn1a

Sox2

Dkk1

E14.5

Sox2

Cdkn1a

Dkk1

d

Lef1

Ptch1

EdU

E14.5

Lef1

Ptch1

EdU

Lef1 or *Ptch1* Level

400

300

200

100

0

****

****

**

ns

Lef1

Ptch1

LD

UD

Peri DC (*Dkk1+*)

DC (*Sox2+*)

Proliferation

%EdU

80

60

40

20

0

***

ns

****

ns

*

0 1 2 3 4

Lef1 level (bin)

E14.0-E14.5

Wnts

Wnts

Wnts

SHH

Upper Dermis (UD)

Lower Dermis

G0 (Queiescent) cell

G1 cell

Proliferating cell

DC cell (*Sox2+*)

Peri-DC cell (*Dkk1+*)

Other UD cell

e **How does a sharp cell-type border form by overlapping Wnt and SHH gradients?**

E14.5 Cell types

UD PeriDC DC

Source

Cell-type Responses:

DC genes

Cell cycle arrest

Peri-DC-to-DC transition

Synchronized temporal progression

Wnt/SHH Activity

DC genes

Cell-type Transition

Sharp border

Wnt/SHH Activity

Cell cycle arrest

Cell-type Transition

Fig. 2

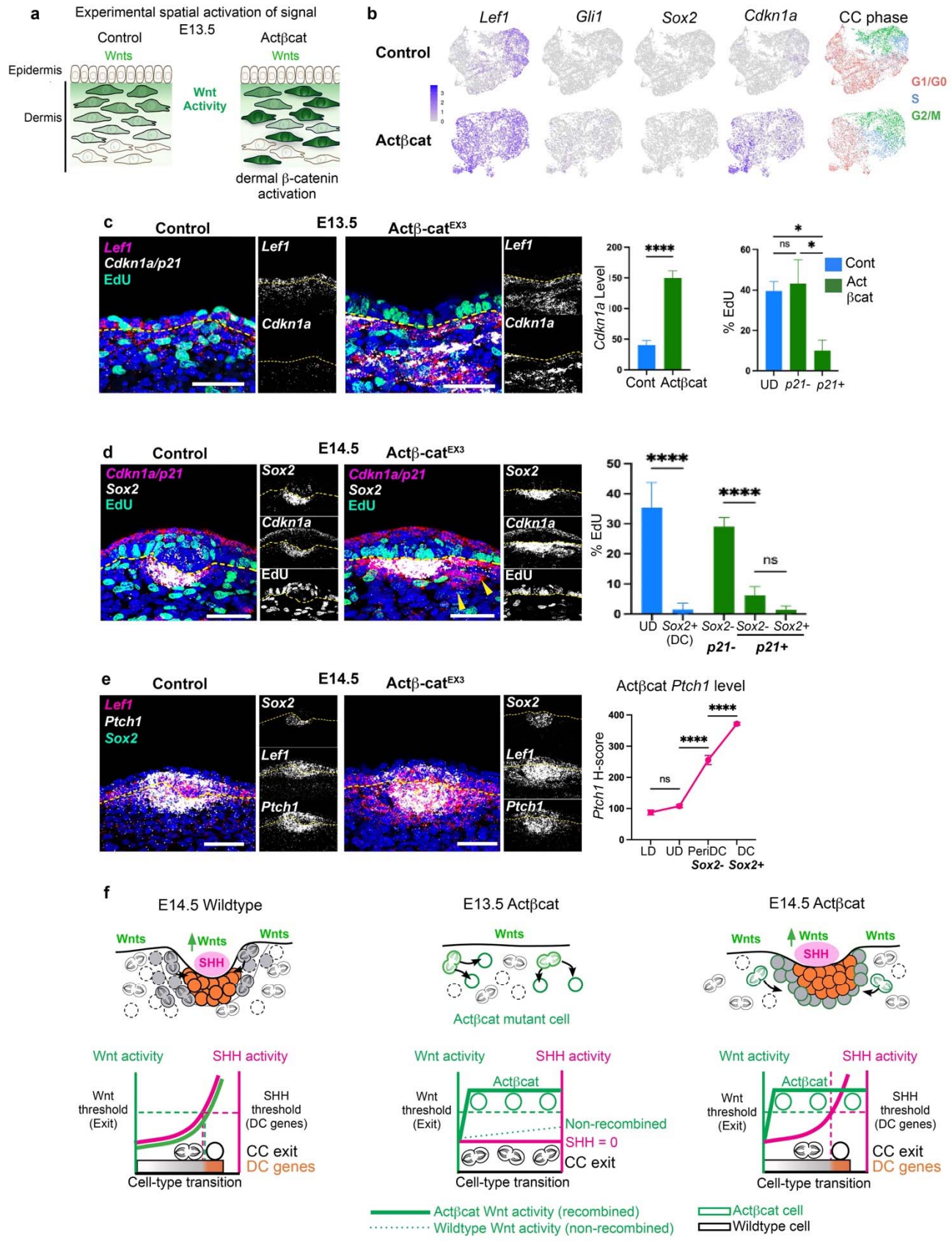
a
Experimental spatial activation of signal
E13.5
Control
Actβcat
Wnts
Epidermis
Dermis
Wnt Activity
dermal β-catenin activation
b
Lef1
Gli1
Sox2
Cdkn1a
CC phase
Control
Actβcat
G1/G0
S
G2/M
c
Control
E13.5
Actβ-catEX3
Lef1
Cdkn1a/p21
EdU
Cdkn1a
Cdkn1a Level
Cont
Actβcat
% EdU
UD
p21-
p21+
ns
d
E14.5
Sox2
EdU
UD
Sox2+ (DC)
Sox2-
p21-
p21+
e
Ptch1
Actβcat Ptch1 level
Ptch1 H-score
LD
PeriDC
DC
Sox2-
Sox2+
f
E14.5 Wildtype
E13.5 Actβcat
E14.5 Actβcat
SHH
Actβcat mutant cell
Wnt activity
SHH activity
Wnt threshold (Exit)
SHH threshold (DC genes)
CC exit
DC genes
Cell-type transition
Non-recombined
SHH = 0
Actβcat Wnt activity (recombined)
Wildtype Wnt activity (non-recombined)
Actβcat cell
Wildtype cell

Fig. 3

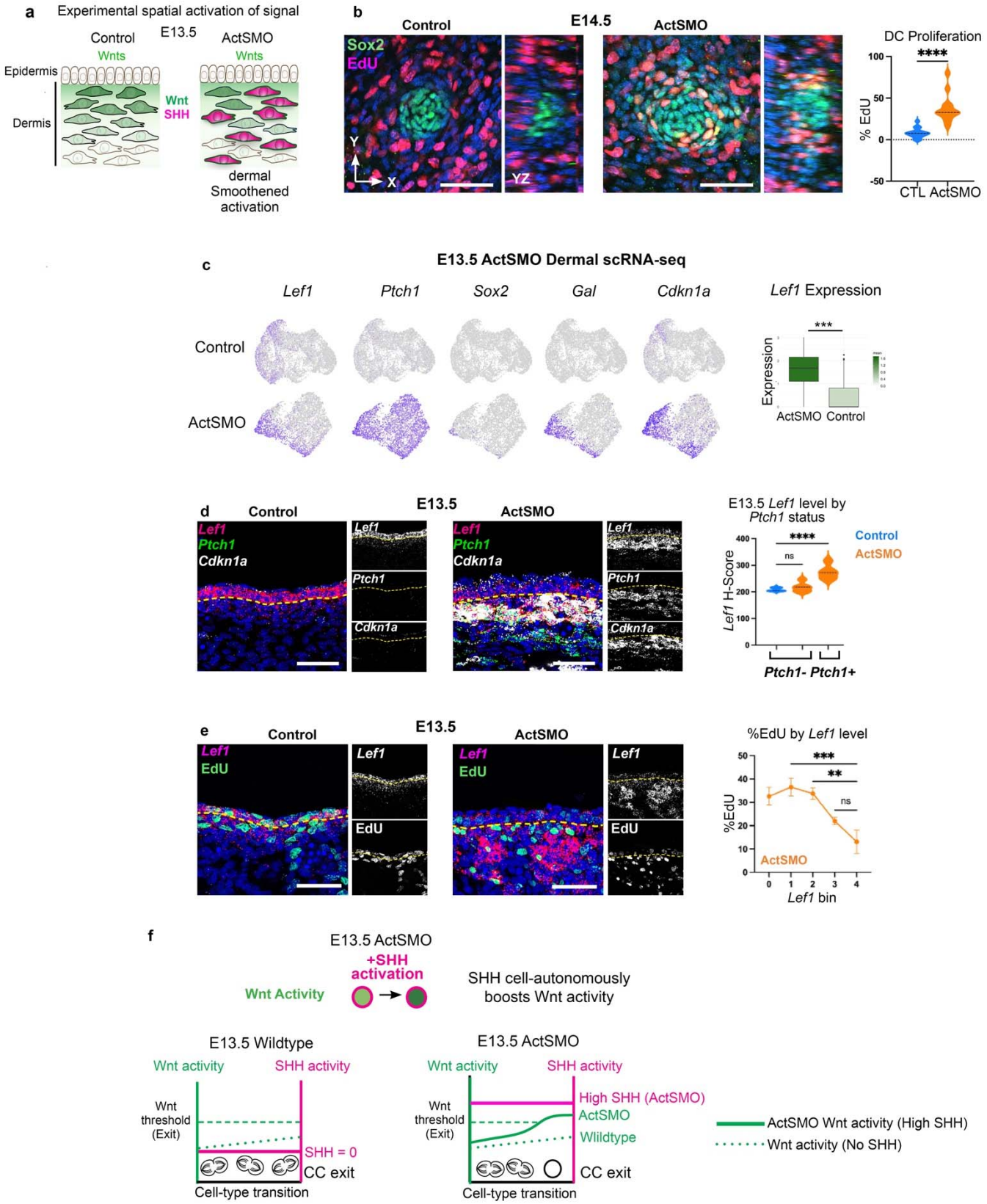

Uniform SH activation increases Wnt output cell-autonomously enabling cells with higher baseline Wnt activity to reach the threshold required for cell-cycle exit

Fig. 4

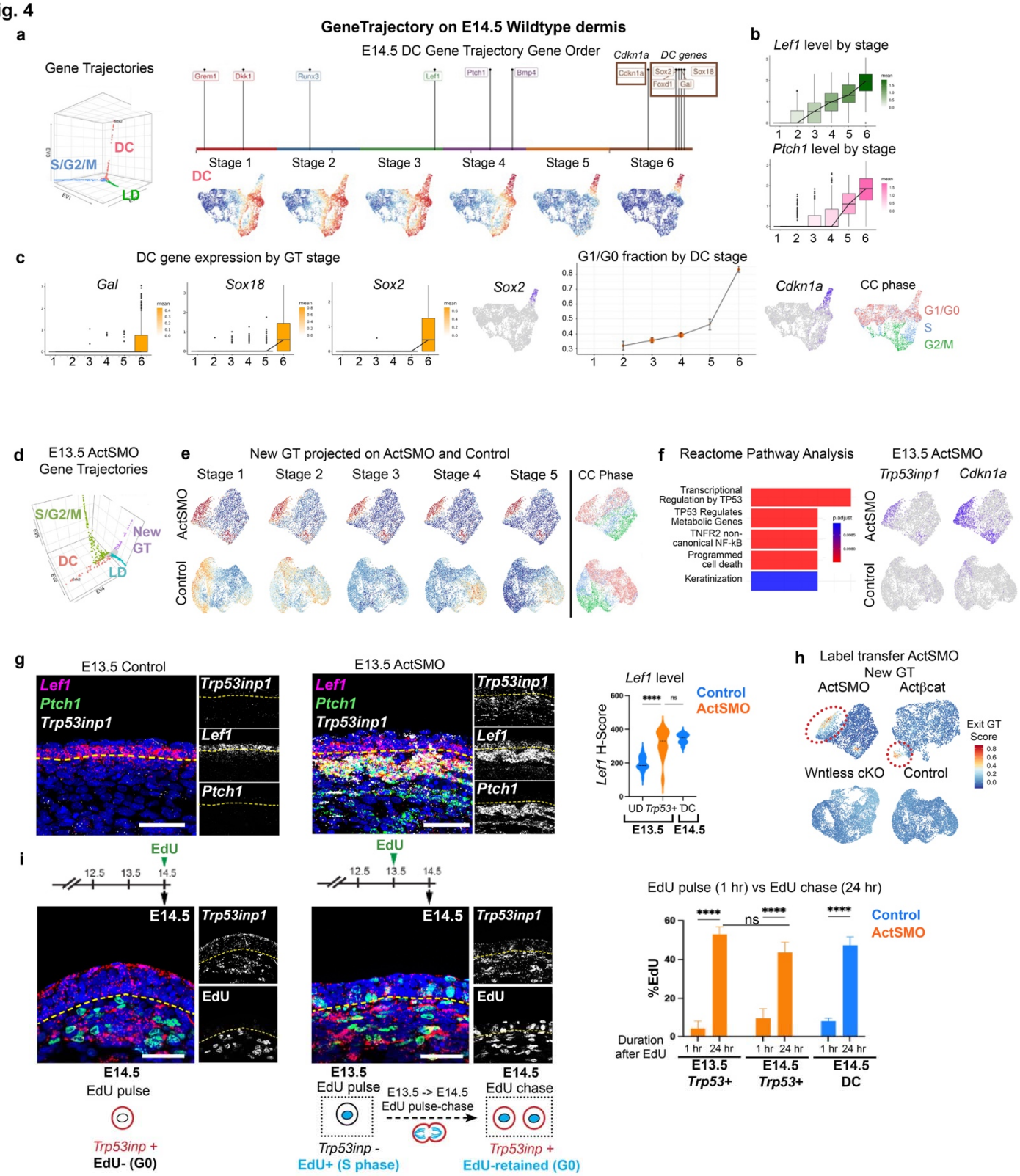
a
GeneTrajectory on E14.5 Wildtype dermis
Gene Trajectories
S/G2/M
DC
LD
E14.5 DC Gene Trajectory Gene Order
Grem1
Dkk1
Runx3
Lef1
Ptch1
Bmp4
Cdkn1a
DC genes
Sox2
Sox18
Foxd1
Gal
Stage 1
Stage 2
Stage 3
Stage 4
Stage 5
Stage 6
b
Lef1 level by stage
Ptch1 level by stage
c
DC gene expression by GT stage
Gal
Sox18
Sox2
G1/G0 fraction by DC stage
Cdkn1a
CC phase
G1/G0
S
G2/M
d
E13.5 ActSMO
Gene Trajectories
New GT
e
New GT projected on ActSMO and Control
ActSMO
Control
CC Phase
f
Reactome Pathway Analysis
Transcriptional Regulation by TP53
TP53 Regulates Metabolic Genes
TNFR2 non-canonical NF-kB
Programmed cell death
Keratinization
p.adjust
E13.5 ActSMO
Trp53inp1
Cdkn1a
g
E13.5 Control
E13.5 ActSMO
Lef1
Ptch1
Trp53inp1
Lef1 level
Lef1 H-Score
Control
ActSMO
UD
Trp53+
DC
E13.5
E14.5
h
Label transfer ActSMO
New GT
ActSMO
Actβcat
Exit GT Score
Wntless cKO
Control
i
EdU
12.5
13.5
14.5
E14.5
EdU
EdU pulse (1 hr) vs EdU chase (24 hr)
%EdU
Duration after EdU
1 hr
24 hr
E13.5 Trp53+
E14.5 Trp53+
E14.5 DC
ns
E14.5
EdU pulse
Trp53inp +
EdU- (G0)
E13.5
EdU pulse
E13.5 -> E14.5
EdU pulse-chase
Trp53inp -
EdU+ (S phase)
E14.5
EdU chase
Trp53inp +
EdU-retained (G0)

Fig. 5

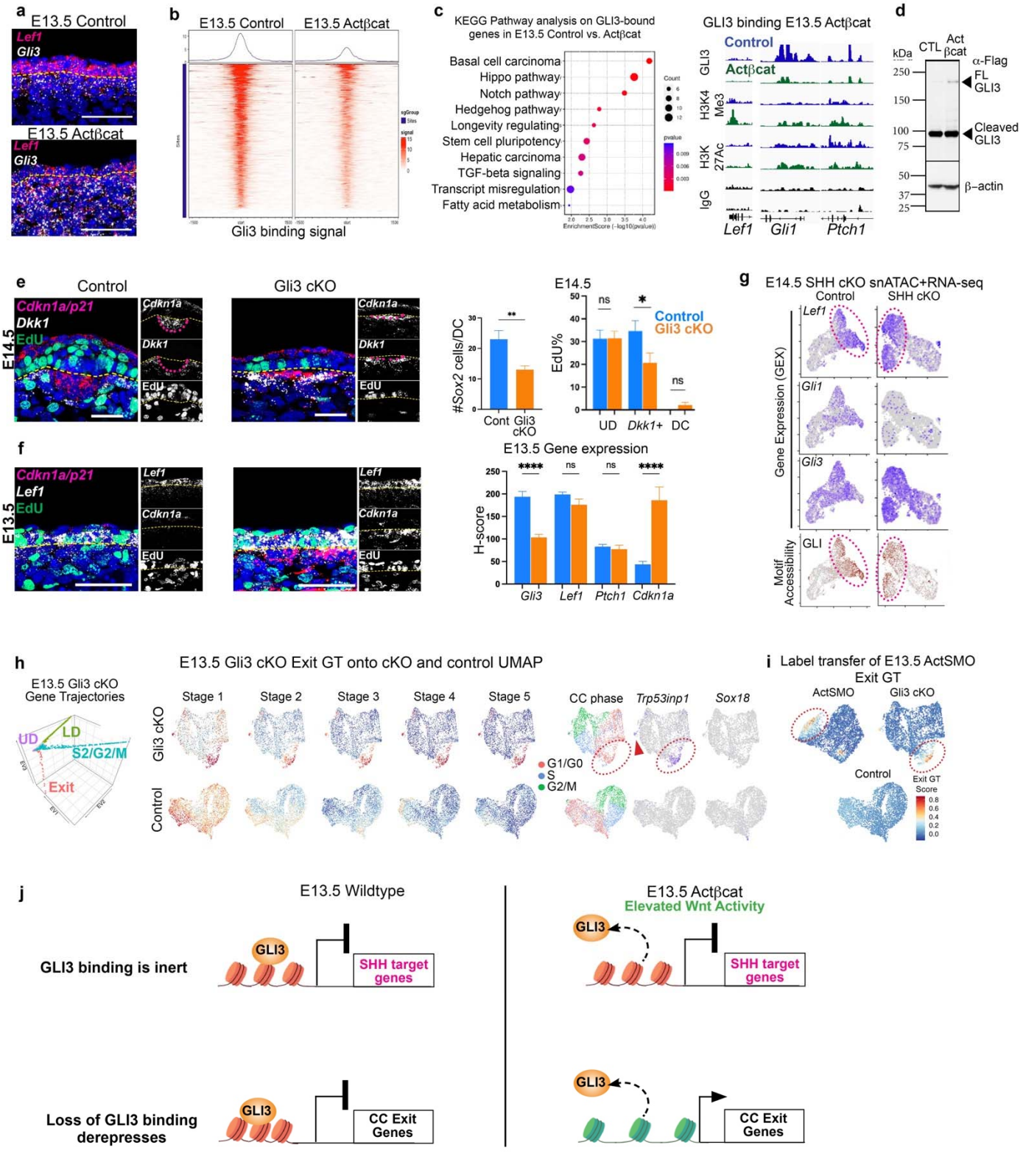
a
E13.5 Control
Lef1
Gli3
E13.5 Actβcat
Lef1
Gli3
b
E13.5 Control
E13.5 Actβcat
Gli3 binding signal
c
KEGG Pathway analysis on GLI3-bound genes in E13.5 Control vs. Actβcat
Basal cell carcinoma
Hippo pathway
Notch pathway
Hedgehog pathway
Longevity regulating
Stem cell pluripotency
Hepatic carcinoma
TGF-beta signaling
Transcript misregulation
Fatty acid metabolism
GLI3 binding E13.5 Actβcat
Control
Actβcat
GLI3
H3K4 Me3
H3K 27Ac
IgG
Lef1
Gli1
Ptch1
d
kDa
CTL
Act βcat
α-Flag
FL GLI3
Cleaved GLI3
β-actin
250
150
100
75
50
37
25
e
Control
Gli3 cKO
E14.5
Cdkn1a/p21
Dkk1
EdU
Cdkn1a
Dkk1
EdU
#Sox2 cells/DC
Cont
Gli3 cKO
E14.5
EdU%
Control
Gli3 cKO
UD
Dkk1+
DC
ns
*
**
f
E13.5
Cdkn1a/p21
Lef1
EdU
Cdkn1a
EdU
E13.5 Gene expression
H-score
Gli3
Lef1
Ptch1
Cdkn1a
****
ns
g
E14.5 SHH cKO snATAC+RNA-seq
Control
SHH cKO
Lef1
Gli1
Gli3
Gene Expression (GEX)
GLI
Motif Accessibility
h
E13.5 Gli3 cKO Exit GT onto cKO and control UMAP
E13.5 Gli3 cKO Gene Trajectories
UD
LD
S2/G2/M
Exit
Stage 1
Stage 2
Stage 3
Stage 4
Stage 5
CC phase
Trp53inp1
Sox18
Gli3 cKO
Control
G1/G0
S
G2/M
i
Label transfer of E13.5 ActSMO Exit GT
ActSMO
Gli3 cKO
Control
Exit GT Score
j
E13.5 Wildtype
E13.5 Actβcat
Elevated Wnt Activity
GLI3 binding is inert
GLI3
SHH target genes
Loss of GLI3 binding derepresses
CC Exit Genes

Fig. 6

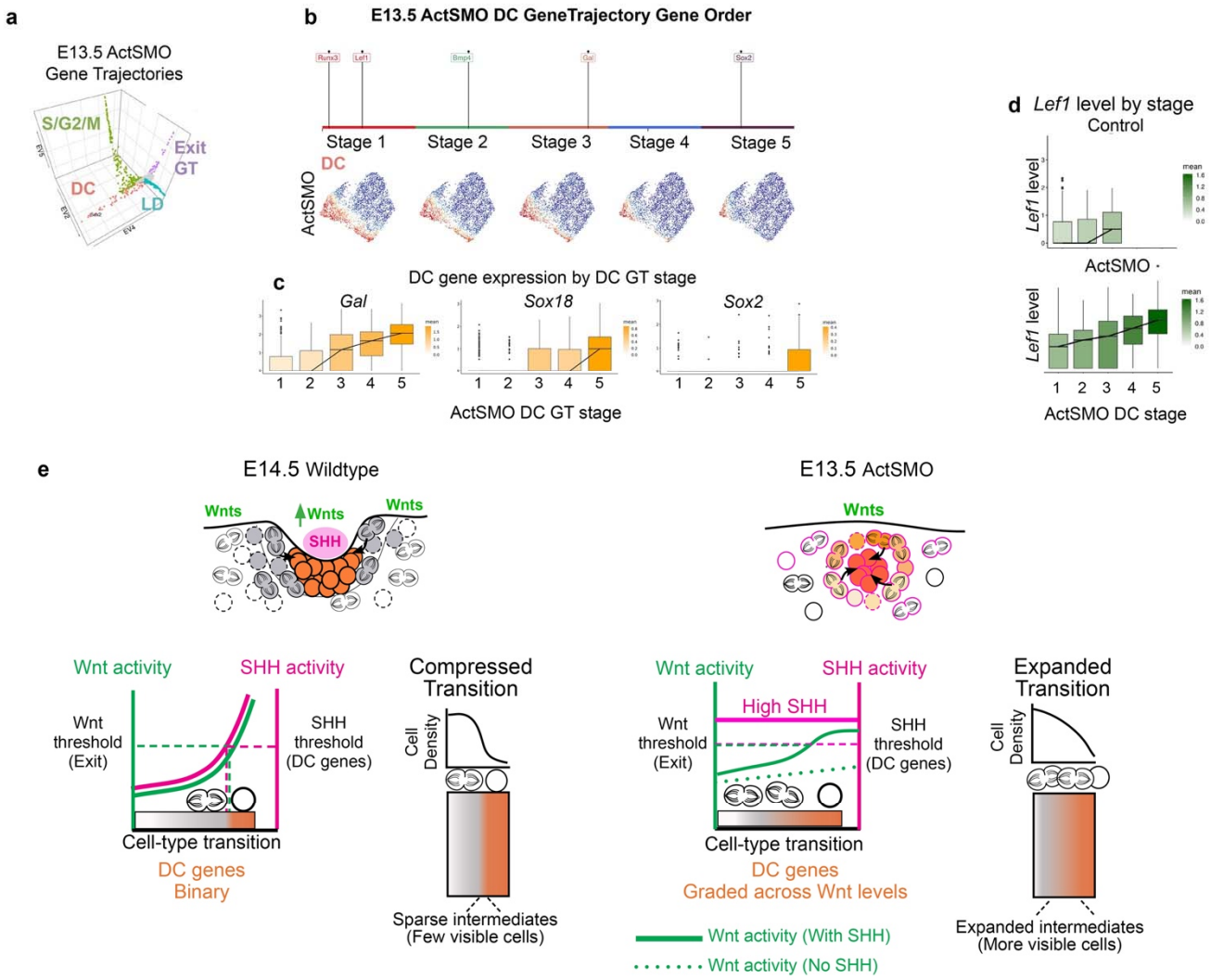

Coupling of Wnt-dependent cell-cycle exit with SHH-driven differentiation prevents proliferative expansion of intermediate states, restricting their accumulation during the transition

Fig. 7

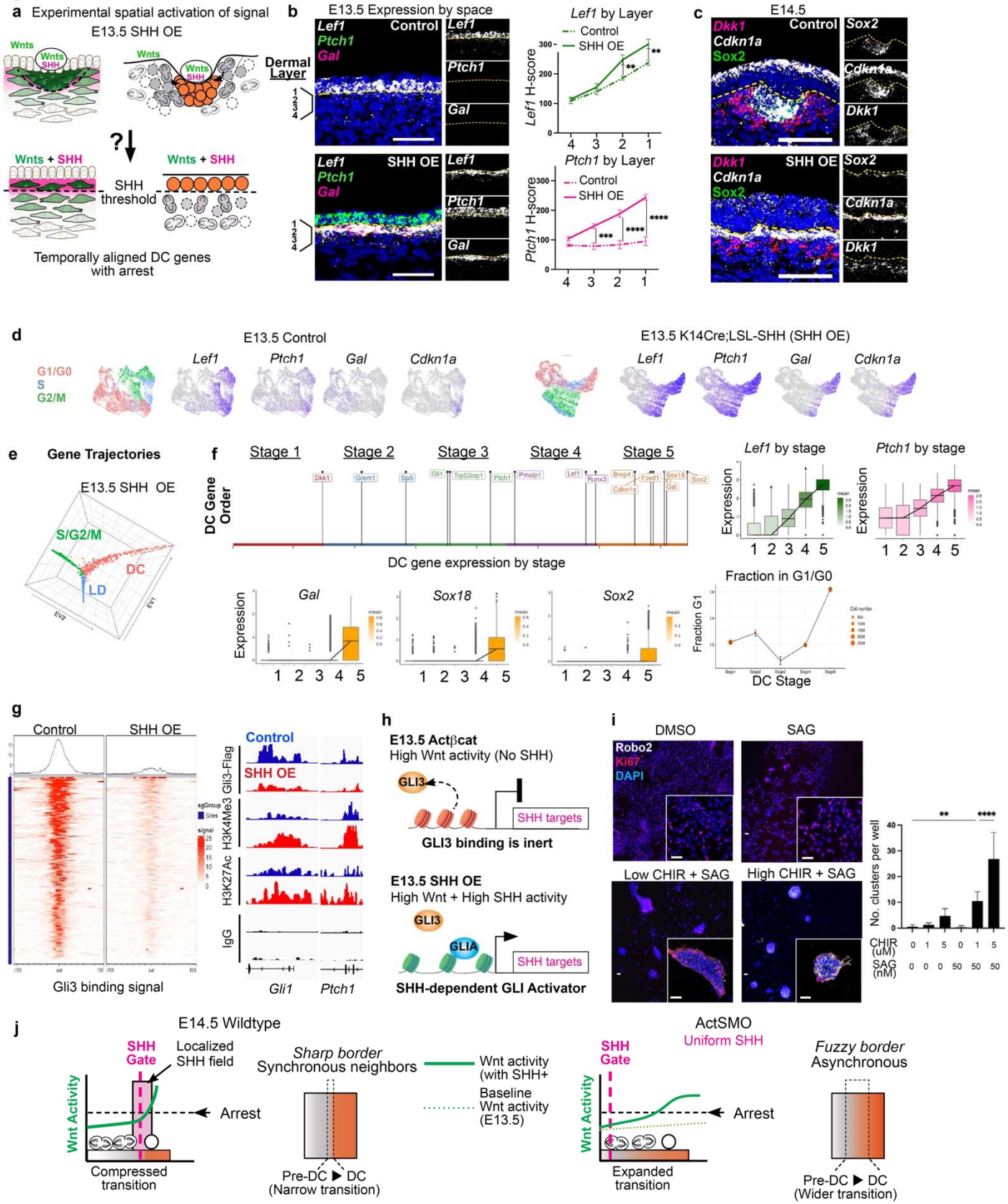
a Experimental spatial activation of signal
E13.5 SHH OE
Wnts
Wnts SHH
Dermal Layer
Wnts + SHH
SHH threshold
Temporally aligned DC genes with arrest
b E13.5 Expression by space
Lef1
Ptch1
Gal
Control
SHH OE
Lef1 by Layer
Ptch1 by Layer
Lef1 H-score
Ptch1 H-score
c E14.5
Dkk1
Cdkn1a
Sox2
d E13.5 Control
E13.5 K14Cre;LSL-SHH (SHH OE)
G1/G0
S
G2/M
Cdkn1a
e Gene Trajectories
E13.5 SHH OE
S/G2/M
DC
LD
f Stage 1
Stage 2
Stage 3
Stage 4
Stage 5
DC Gene Order
DC gene expression by stage
Lef1 by stage
Ptch1 by stage
Expression
Gal
Sox18
Sox2
Fraction in G1/G0
Fraction G1
DC Stage
g Control
SHH OE
Gli3-Flag
H3K4Me3
H3K27Ac
IgG
Gli3 binding signal
Gli1
Ptch1
h E13.5 Actβcat
High Wnt activity (No SHH)
GLI3
SHH targets
GLI3 binding is inert
E13.5 SHH OE
High Wnt + High SHH activity
GLIA
SHH-dependent GLI Activator
i DMSO
SAG
Robo2
Ki67
DAPI
Low CHIR + SAG
High CHIR + SAG
No. clusters per well
CHIR (uM)
SAG (nM)
j E14.5 Wildtype
SHH Gate
Localized SHH field
Wnt Activity
Arrest
Compressed transition
Sharp border
Synchronous neighbors
Pre-DC ▶ DC
(Narrow transition)
Wnt activity (with SHH+
Baseline Wnt activity (E13.5)
ActSMO
Uniform SHH
Expanded transition
Fuzzy border
Asynchronous
Pre-DC ▶ DC
(Wider transition)
Local SHH synchronizes cell-cycle exit + differentiation
Differentiation without synchronized exit